Analysis of the Impact of Geomagnetic Storm Onset Time on GNSS Signal Reliability

Tumuhairwe Bruce
BU/GS22/MSP/3

A dissertation submitted to the Directorate of Graduate Studies, Research and Innovations in partial fulfillment of the requirements for the award of a Degree of Master of Science in Physics of Busitema University

October 2025

Declaration

I the undersigned, declare that this Dissertation is as a result of my own effort, my original work and that it has never been submitted by anyone to any institution of higher learning for any academic award.

Name: Tumuhairwe Bruce

Signature: 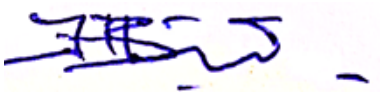

Date: 3/11/2025

Approval

The dissertation titled: **Analysis of the Impact of Geomagnetic Storm Onset Time on GNSS Signal Reliability** is submitted in partial fulfillment for the award of a Degree of Master of Science in Physics of Busitema University, with the approval of the following academic supervisors:

Name: Dr. Abiriga Faustine

Signature: 

Date: 3/11/2025

Name: Ass. Prof. Emirant Amabayo

Signature: 

Date: 3/11/2025

Dedication

I dedicate this project to my late father, Tibasiima Ezekiel, and my mother, Enid Muhairwe, for raising and educating me.

Acknowledgement

I express my sincere gratitude to the Almighty God for the gift of life, good health and divine protection throughout the course of this study.

I am profoundly grateful to my supervisors, Dr. Abiriga Faustine and Assoc. Prof. Emirant Amabayo for their continuous guidance, insightful advice and invaluable contributions which have shaped the direction and quality of this research. Your mentorship has been instrumental in my academic journey.

Special appreciation goes to Dr. Geoffrey Andima for his exceptional support throughout this process. He consistently helped me to refine and strengthen my work.

I also extend my heartfelt thanks to my coursemates, colleagues and all my friends for their constant encouragement, companionship, constructive feedback and the many forms of support you offered during this academic endeavor. Your contributions have been deeply appreciated and will always be remembered.

Lastly I wish to sincerely thank my wife, Ntono Irene, for all the support she rendered to me during this study. She always stood in the gap whenever I was away and kept our family in order.

Contents

List of Figures

List of Tables

Abbreviations and Acronyms

CIR:	Corotating Interaction region
CMEs:	Coronal Mass Ejections
CNR:	Carrier-to-noise-Ratio
DCB:	Differential Code Bias.
DDEF:	Disturbance Dynamo Electric Field
Dst:	Disturbance storm time index.
EIA:	Equatorial Ionization Anomally
EUV:	Extreme Ultraviolet
GLONASS:	Globalnaya Navigazionnaya Sputinikovaya Sistema
GNSS:	Global Navigation Satellite System
GPS:	Global Positioning System
ICME:	Interplanetary Coronal Mass Ejection.
IGS:	International GNSS Service.
IMF:	Interplanetary Magnetic field.
ISM:	International Scintillation Monitor.
Kp:	Planetary K Index
MEO:	Medium Earth Orbit
MHD:	Magnetohydrodynamic
PPED:	Prompt Penetration Electric Field
PRE:	Pre-reversal Enhancement
PRN:	Pseudo Random Number
RE:	Earth Radius
RTI:	Rayleigh Taylor Instability
SATCOM:	Satellite Communication
SCINDA:	SCintillation Network Decision Aid
SEPs:	Solar Energetic Particles
SNR:	Signal-to-Noise-Ratio
SSC:	Sudden Storm Commencement.
TEC:	Total Electron Content.
USA:	United States of America.
UT:	Universal Time.
UV:	Ultraviolet
VHF:	Very High Frequency

Symbols and Notations

H: Neutral Hydrogen.
H^+**:** Hydrogen ion
He: Neutral Helium
O: Neutral Atomic Oxygen
He^+**:** Helium ion
O^+**:** Atomic Oxygen Ion
O_2**:** Neutral Oxygen Molecule
O_2^+**:** Oxygen Molecule Ion
O_2^-**:** Negative Oxygen Molecule Ion
N: Neutral Atomic Nitrogen
N^+**:** Nitrogen ion
N_2**:** Neutral Nitrogen molecule
N_2**+:** Nitrogen molecule ion
NO: Neutral Nitric oxide
NO^+**:** Nitric Oxide ion
NO^2**:** Neutral Nitrogen Dioxide
e: Electron charge
*ne***:** Electron density

Abstract

This study investigates the effects of geomagnetic storm onset time on the performance of Global Navigation Satellite System (GNSS). Unlike previous studies focusing primarily on storm intensity, this work establishes storm onset time as a key predictive parameter for ionospheric scintillation occurrence. The analysis uses geomagnetic storm data and Global Positioning System (GPS) scintillation data from two low-latitude stations, Makerere and Mbarara, spanning 2011 to 2016. A total of 1,082 geomagnetic storms were identified and classified by their intensity into weak (-50 nT $\leq$ Dst < -25 nT), moderate ($-100 < Dst \leq -50$ nT), and severe ($Dst \leq -100$ nT) categories. Only a minority of storms triggered ionospheric scintillation, indicating that storm intensity alone is insufficient to predict scintillation events. Scintillation was identified using the amplitude index (S4), with thresholds set between 0.2 and 1.2. Using the epoch of minimum IMF Bz (bow shock time) as the precise storm onset marker, results show that scintillation predominantly occurred during night hours. Strong scintillation was observed consistently when the bow shock time fell between 15:00 UT and 00:00 UT (evening to nighttime in East Africa's low-latitude region), with weaker events between 12:00 UT and 15:00 UT. No scintillation was detected when storm onset occurred from 00:00 UT to 12:00 UT, even during severe storms. These findings highlight the critical role of storm commencement timing in ionospheric irregularity development and subsequent GNSS signal degradation, which is crucial for mitigating risks in aviation, communication, and navigation systems in low-latitude regions.

Chapter 1

Introduction

1.1 Background

Geomagnetic storms are natural disturbances driven by solar activity and represent one of the most significant phenomena affecting satellite navigation systems. These storms result from complex interactions between the solar wind streams of charged particles from the Sun and Earth's magnetosphere, which acts as a protective shield. The solar wind can disturb Earth's magnetic field, causing geomagnetic storms characterized by increased auroral activity, disruptions in radio communications, and satellite operation disturbances (Kintner and Ledvina, 2005). As societies increasingly rely on the Global Positioning System (GPS) for navigation, mapping, and time synchronization across various sectors, understanding the effects of geomagnetic storms is critical to maintaining satellite navigation reliability and accuracy.

The ionosphere, a region of the upper atmosphere rich in charged particles, plays a crucial role in satellite navigation by reflecting and refracting radio signals. Geomagnetic storms induce rapid changes in the ionosphere, increasing electron density and generating irregularities that distort GPS signals. These disturbances cause signal delays that degrade navigation accuracy and can lead to outages. Studies show that the Total Electron Content (TEC) of the ionosphere can rise significantly during geomagnetic storms, directly correlating with GPS signal degradation (Kintner and Ledvina, 2005). Low-latitude regions, such as Uganda and East Africa, experience frequent and intense ionospheric scintillations primarily due to complex plasma processes unique to these areas. A key driver of this is the Rayleigh-Taylor Instability (RTI), a plasma instability that occurs after sunset in the equatorial ionosphere. RTI causes the formation of large-scale plasma depletions known as plasma bubbles. These bubbles rise through the ionosphere, creating strong electron density irregularities that scatter and distort trans-ionospheric radio signals (Akala et al., 2015). These conditions amplify the impact of geomagnetic storms on satellite signals, creating a pressing need for region-specific research.

A critical yet underexplored factor influencing scintillation occurrence and navigation reliability is the timing of geomagnetic storm onset. While most studies emphasize storm intensity, few address how the storm commencement time affects ionospheric irregularities and GNSS performance. This research gap motivates the present study, which investigates the role of storm commencement timing in ionospheric scintillation at low latitudes. The Figure 1.1 presents a comprehensive overview of space weather related events and their

impacts on Earth, highlighting the broad consequences across different domains:

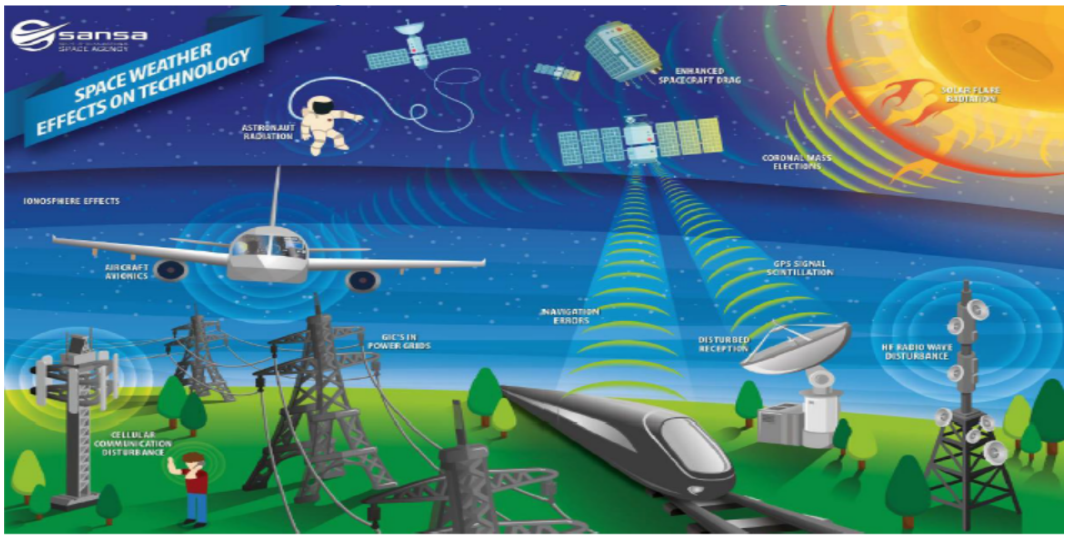

Figure 1.1: A systematic overview of the space weather related events *Adapted from Dumbović (2015)*

As illustrated in Figure 1.1, aviation, marine navigation, military operations, and economic activities rely heavily on GPS. Disruptions caused by geomagnetic storms can result in navigation errors, threatening flight safety, safe passage through congested waterways, strategic military operations, and logistics efficiency (Huang et al., 2016a). Despite advances such as real-time space weather monitoring and forecasting by organizations like NOAA and USGS, current mitigation strategies remain insufficient. There is a growing need to develop robust navigation algorithms that compensate for ionospheric disturbances and explore machine learning approaches that adapt in real time to improve navigation reliability during geomagnetic storms. Therefore, this study aims to deepen understanding of geomagnetic storm onset effects on satellite navigation and contribute to effective mitigation solutions tailored for vulnerable low-latitude regions.

1.2 Problem statement

The increasing reliance on Global Navigation Satellite System (GNSS) for critical applications has made understanding ionospheric disturbances caused by geomagnetic storms a pressing research priority. Many previous studies have linked scintillation events mainly to the strength of geomagnetic storms using indices such as K-planetary (Kp) and Disturbed Storm Time (Dst). However, these intensity-based indices have often overlooked the critical factor of storm onset time. This limitation reduces the ability of existing predictive models to explain variations in scintillation patterns, particularly in the low-latitude region of East Africa. This gap is especially problematic as the region experiences strong equatorial ionization anomalies and frequent post-sunset scintillations.

1.3 Aim

To analyse the impact of geomagnetic storm onset time on GNSS reliability.

1.4 Specific objectives

The specific objectives of this research included:

1. Characterisation of geomagnetic storms during the 24th solar cycle.
2. Identification of ionospheric scintillations during the period of study.
3. Determine the correlation between time of commencement of geomagnetic storms and signal scintillation events.

1.5 Scope

This study analyzes geomagnetic storm data, including Dst, Kp, and interplanetary magnetic field (IMF) Bz indices, alongside GPS scintillation data recorded between 2011 and 2016. The scintillation measurements were obtained from GPS SCINDA receivers located in two low-latitude stations in Uganda at Mbarara (MBA) and Makerere (MAK). While focused on these Uganda sites, the findings are intended to be representative of broader low-latitude and equatorial regions in East Africa, where similar ionospheric phenomena occur. The study uses the epoch of minimum IMF Bz (bow shock time) to precisely define geomagnetic storm onset, allowing detailed examination of how onset timing correlates with scintillation occurrences. However, it does not model all storm drivers such as coronal mass ejections (CMEs) or corotating interaction regions (CIRs), nor does it consider other sources of GNSS errors like multipath effects or tropospheric delays. Although correlations between storm onset timing and scintillation activity are identified, this research does not develop operational forecasting models for real-time GNSS prediction. The scope is limited to improving the physical understanding of storm timing effects on ionospheric irregularities in low-latitude East Africa, providing foundational knowledge to support future development of mitigation strategies.

1.6 Significance

Unlike existing studies that focus primarily on geomagnetic storm intensity, this research demonstrates that storm commencement time specifically the bow shock time critically influences GNSS scintillation disruptions in the equatorial and low-latitude regions of East Africa. By incorporating storm onset timing as a key parameter alongside traditional intensity indices, this study fills a significant gap in space weather literature and improves the understanding of temporal factors affecting ionospheric irregularities in this understudied region. The unique findings highlight the diurnal dependence of scintillation

activity on storm onset, providing new insights tailored to the equatorial ionization anomaly environment prevalent in East Africa. This knowledge advances theoretical models of ionospheric plasma dynamics and offers practical implications for improving GNSS reliability. Sectors such as aviation, maritime navigation, telecommunications, and emergency response in East Africa stand to benefit directly from these results. Policymakers, GNSS service providers, airline operators, and space weather researchers can use this information to enhance forecasting accuracy and implement more effective mitigation strategies. In the long term, these findings can feed into the development of more resilient GNSS systems and regional space weather monitoring frameworks, strengthening infrastructure critical to national security, economic development, and public safety in low-latitude countries.

Chapter 2

Literature Review

2.1 The sun and its activities

According to Kivelson and Russell (1995), the Sun is a massive, magnetized gaseous body at the center of our solar system. It has an effective temperature of 5,785 K and a diameter of approximately 1,392,000 km which is 109 times that of Earth (Bahcall et al., 2001). Its mass, about 1.99×10^{30} kg, constitutes nearly 99.86% of the solar system's total (Chernosky and Hagan, 1958). The Sun's composition primarily involves Hydrogen (92.1%) and Helium (7.8%), alongside traces of heavier elements (Bahcall et al., 2001). Structurally, it is divided into interior and exterior regions, each comprising distinct physical layers as shown in Figure 2.1.

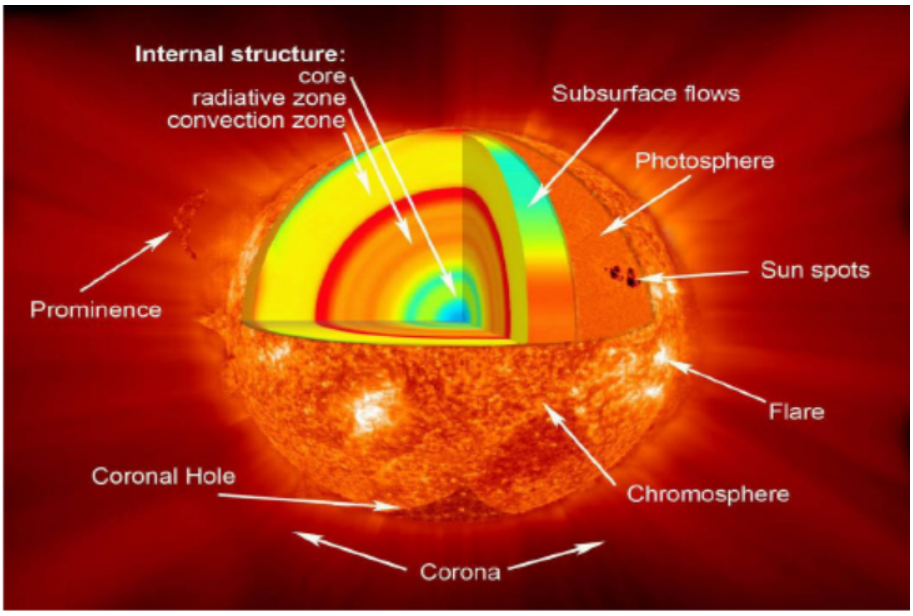

Figure 2.1: The structure of the Sun (interior and exterior regions). *Adapted from Singh (2019)*

Solar energy originates deep in the core from thermonuclear fusion reactions, where extreme pressure and temperature prevail (Bahcall et al., 2001). Energy transport occurs radiatively through the radiation zone, transitioning to convective processes in outer layers (Bray and Loughhead, 1964). The photosphere is the the visible solar surface, it has a temperature of about 5,785 K and a thickness nearly 500 km (Kivelson and Russell, 1995). Notably, sunspots the regions of intense magnetic fields and reduced temperature form on the photosphere, and their magnetic activity is a source of particle acceleration linked to solar events (Chernosky and Hagan, 1958). Above the photosphere, the chromosphere and the extremely hot solar corona extend outward, with the corona

exhibiting temperatures of several million Kelvin and hosting solar prominences related to sunspot activity (Bahcall et al., 2001; Aschwanden, 2005; Bray and Loughhead, 1964).

2.1.1 Sunspot and Solar Cycle

Sunspots, characterized by stronger magnetic fields suppressing convection, appear darker and last on average about 10 days, with sizes ranging substantially (Prölss and Prölss, 2004; Bray and Loughhead, 1964). Their formation predominantly occurs within $\pm 30^{\circ}$ solar latitude (Tandberg-Hanssen, 1995), covering less than 1% of the solar surface at any time. The sunspot population varies cyclically over approximately 11 years, defining periods of solar maximum and minimum (Aschwanden, 2005). These cycles correlate with heightened solar activity, influencing space weather phenomena relevant to geomagnetic disturbances.

2.1.2 Solar Flare

Solar flares are short-lived bursts of electromagnetic radiation caused by magnetic energy release near sunspots, accelerating particles and affecting Earth's ionosphere by enhancing the D-layer and disrupting radio communications (Bray and Loughhead, 1964; Carrington, 1863; Thomas and Teske, 1971). Their rapid arrival at Earth, traveling at light speed, distinguishes them from other solar phenomena (Carrington, 1863).

2.1.3 Coronal Mass Ejection

Coronal Mass Ejections (CMEs) are large-scale expulsions of magnetized plasma propelled from the Sun's surface by magnetic field fluctuations (Harrison et al., 1990; Hundhausen, 1999). Traveling at speeds up to 1000 km/s and carrying substantial mass, CMEs generate shocks that accelerate solar energetic particles and trigger geomagnetic storms upon interacting with Earth's magnetosphere, particularly when the IMF Bz component is southward (Gopalswamy, 2017; Hundhausen, 1999). Halo CMEs, directed toward Earth, are especially geoeffective and represent major drivers of space weather impacts on satellite and GNSS systems (Gopalswamy et al., 2009; Center, 2023).

2.1.4 Corotating Interaction Regions

CIRs form where fast solar wind streams from coronal holes interact with slower ambient flows, producing compression regions that can induce moderate geomagnetic disturbances (Tsurutani et al., 2003; Balogh et al., 1992). Coronal holes, often located near solar poles, are sources of these high-speed streams (700–800 km/s) and significantly influence geomagnetic activity, especially during solar minimum phases (Bray and Loughhead, 1964; Cranmer, 2009).

2.2 Solar wind and Interplanetary Magnetic Field

According to Parker (1965); Kelly et al. (2012), the Sun continuously emits highly conducting plasma from the corona, driven by gravity and temperature gradients (Owens and Forsyth, 2013). This plasma, composed primarily of protons, electrons, and about 5% helium ions, escapes the Sun's gravity due to the corona's high temperature and flows outward as the solar wind (Owens and Forsyth, 2013), reaching speeds commonly between 300 and 1500 km/s, averaging about 500 km/s. Typical solar wind properties include electron densities near 5 particles/cm^3, proton densities around 6.6 particles/cm^3, electron temperatures of approximately $1.2 \times 10^5 K$, and magnetic fields averaging 10 nT (Treumann and Baumjohann, 1997). The solar wind carries the Sun's magnetic field into interplanetary space, known as the interplanetary magnetic field (IMF) (Parker, 1958). Due to solar rotation, the IMF adopts a spiral shape stemming from regions with open magnetic field lines (Parker, 1965; Kelly et al., 2012). The IMF's orientation critically influences Earth's magnetosphere configuration and geomagnetic activity (Owens and Forsyth, 2013; Wang et al., 2007). It is decomposed into orthogonal components Bx, By, and Bz The Bz component representing the north-south direction is particularly significant (Parker, 1958). A sustained southward IMF Bz (negative values) is identified as the most geoeffective condition for triggering geomagnetic storms due to enhanced magnetic reconnection at the dayside magnetopause (Parker, 1965; Kelly et al., 2012; Wang et al., 2007). While thresholds such as a sustained IMF Bz below -10 nT for several hours have been proposed to predict storm onset, uncertainties remain regarding the variability of storm responses and regional differences (Pulkkinen et al., 2010). At equatorial latitudes like East Africa, prolonged southward IMF Bz intensifies prompt penetration electric fields into the ionosphere, exacerbating ionospheric irregularities and scintillation activity critical to GNSS performance (Kintner et al., 2007b).

2.3 The Earth's Atmosphere

The Earth's atmosphere extends from sea level up to about 1000 km altitude and consists of a mixture of gases and particles, with 99% of its mass below 30 km (Parker, 1958; Memarzadeh, 2009). It is structured into concentric layers primarily defined by altitude, temperature gradients, and particle composition (Owens and Forsyth, 2013; Gradwell, 2006). A key transition called a "pause" marks where one layer's characteristics shift to the next. The atmosphere's four principal layers are the troposphere, stratosphere, mesosphere, and thermosphere (Memarzadeh, 2009). Often excluded from this standard stratification is the exosphere, extending roughly from 500 to 1000 km, where atmospheric pressure is extremely low and collisions between particles rare (Borduas and Donahue, 2018; Schunk and Nagy, 2009). Composed mainly of hydrogen and helium, the exosphere is where incoming solar radiation first interacts with Earth's atmosphere (Laštovička

et al., 2006; He et al., 2003).The thermosphere, often synonymous with the ionosphere, spans approximately 90 to 500 km and features ions created by photoionization (Schunk and Nagy, 2009). This layer's temperature increases with altitude, influencing the propagation of radio signals critical for satellite-based navigation (Memarzadeh, 2009). Beneath it, the mesosphere (50–90 km) cools with altitude and is less stratified than other layers (Schunk and Nagy, 2009; Laštovička et al., 2006). The stratopause at around 50 km separates the mesosphere and stratosphere, dividing the upper and lower atmosphere (Kelley, 2009a). The stratosphere exhibits a distinctive temperature inversion due to ozone photolysis between 25 and 35 km, where the ozone layer absorbs harmful ultraviolet radiation, playing a vital role in sustaining life on Earth (He et al., 2003; Memarzadeh, 2009). The troposphere, containing most atmospheric water vapor and mass, extends from the surface up to around 18 km near the equator, forming a turbulent layer where weather occurs (Schunk and Nagy, 2009; Laštovička et al., 2006). For ionospheric research and GNSS applications, the thermosphere/ionosphere is critical. Variability in its electron density, especially in low-latitude regions like East Africa affected by the equatorial ionization anomaly (EIA), causes signal delays, refraction, and scintillation in satellite navigation systems (Kelley, 2009a). Understanding the layered structure of the atmosphere and the ionosphere's characteristics is therefore fundamental to analyzing and mitigating GNSS disruptions in this region.

2.4 The Ionospshere

The ionosphere is a part of the upper atmosphere that stretches roughly from 60 to 1000 km above the Earth (Goodman, 2005). It doesn't have definate boundaries but it generally lies within this altitude range. This region becomes ionized when high energy solar radiation, especially extreme ultraviolet (EUV) and X-rays, hits the neutral atoms in the upper atmosphere knocking electrons free and creating ions (Burch et al., 2014). The number of free electrons and ions in the ionosphere is always changing because ions can disappear through chemical reactions or recombine with electrons to form neutral particles. These processes depend on the types of ions present and the current atmospheric conditions (Goodman, 2005).Electron loss mainly occurs via recombination, which takes two forms: radiative recombination (slower) where electrons combine with atomic ions, and dissociative recombination (faster) where molecular ions are involved (Memarzadeh, 2009). Additionally, electron attachment forms negative ions predominantly at lower altitudes with higher neutral densities, though these negative ions are short-lived (Burch et al., 2014). The balance of ion production and loss causes ionospheric electron density to vary over timescales ranging from minutes to years (Biondi, 1969). The ionosphere is subdivided into three principal regions the D, E, and F based on altitude, electron density, and particle composition (Anderson, 1999). The D-region (50–90 km) has electron densities around $10^4/cm^3$ during daytime but largely disappears at night

(Thomson and Clilverd, 2005). It is ionochemically complex due to multiple ionization sources and plays a crucial role in radio wave absorption across MF, HF, and VHF bands (Kintner and Ledvina, 2005). The E-region (90–130 km) reaches daytime electron densities of approximately $10^5/cm^3$, decreasing to about 5×10^3 at night (Schunk and Nagy, 2009). Ionization here is driven mainly by soft X-rays (8–10.4 nm) and ultraviolet radiation (80–102.6 nm), producing dominant ion species such as NO^+ and O_2^+, along with secondary ions (Ratcliffe, 1972; Burch et al., 2014). Above approximately 130 km lies the F-region, extending beyond 600 km, primarily composed of atomic oxygen ions. Unlike the D and E layers, the F region persists at night due to lower recombination rates (Burch et al., 2014). During daytime, it often splits into F1 and F2 regions, with occasional observation of an F3 layer above F2 (Bittencourt and Abdu, 1981). The F-region electron density variability is particularly significant for GNSS signal propagation, as it hosts complex plasma structures responsible for scintillation and total electron content (TEC) fluctuations, especially pronounced in equatorial regions such as East Africa, which exhibit intense ionospheric irregularities linked to the equatorial ionization anomaly.

2.5 The geomagnetic field

The Earth's geomagnetic field is generated by the dynamo effect which arises from the movement of molten iron and nickel in the outer core. This field extends from deep within the inner core out into space forming the magnetosphere that shields our planet by deflecting charged particles from the solar wind and cosmic radiation (Eastwood et al., 2015; Gubbins, 2008; Olson and Christensen, 2006). Fluid motions within the outer core cause the magnetic poles to slowly shift and sometimes even reverse over geological time (Glatzmaier and Roberts, 1995). At any given location, the geomagnetic field is described by parameters such as magnetic declination (D), horizontal intensity (H) and vertical intensity (Z) which are essential for understanding how the field changes across space and time (Burch, 1974). The magnetic equator where a compass needle shows no dip runs roughly parallel to the Earth's geographic equator but slowly shifts, showing just how dynamic the field really is (Adams, 2007). Beyond this classical understanding, processes in the magnetosphere strongly influence ionospheric dynamics near the equator, affecting the reliability of GNSS signals. When the interplanetary magnetic field (IMF) Bz points southward, it triggers magnetic reconnection at the dayside magnetopause, which strengthens convection electric fields that penetrate to the equatorial ionosphere. These prompt penetration electric fields (PPEFs) amplify plasma instabilities, causing equatorial plasma bubbles and irregularities responsible for scintillation (Kelley, 2009a). This coupling is particularly significant in East Africa's low-latitude region, where the equatorial ionization anomaly (EIA) and strong pre-reversal enhancement (PRE) intensify these effects (Eastwood et al., 2015). Understanding how

disturbances in the magnetosphere drive ionospheric irregularities is key to predicting and mitigating GNSS disruptions in this vulnerable region. Overall, this highlights the crucial role of storm-time magnetosphere ionosphere interactions in East Africa's unique near equatorial environment.

2.5.1 Earth's Magnetosphere

The Earth is surrounded by a magnetic field cavity known as the magnetosphere (Gubbins, 2008). This region is dominated by the planet's magnetic field and arises from the interaction between the Earth's magnetic field and the solar wind. The magnetosphere is not fixed; it constantly changes shape due to these solar wind interactions. On the side facing the Sun, it is compressed into a bow-shaped boundary called the magnetopause, while on the night side, it stretches out into a long tail known as the magnetotail (Eastwood et al., 2015). Acting as a vital shield, the magnetosphere protects Earth by deflecting or trapping charged particles from the solar wind, preventing most of them from reaching the surface (Ganushkina et al., 2018). This protection is essential for preserving Earth's atmosphere and supporting life by blocking harmful solar radiation. Within the magnetosphere, complex processes such as magnetic reconnection, particle acceleration, and wave-particle interactions take place, giving rise to phenomena like auroras and geomagnetic storms (Axford, 1962). The systematic structure of the magnetosphere is shown in Figure 2.2

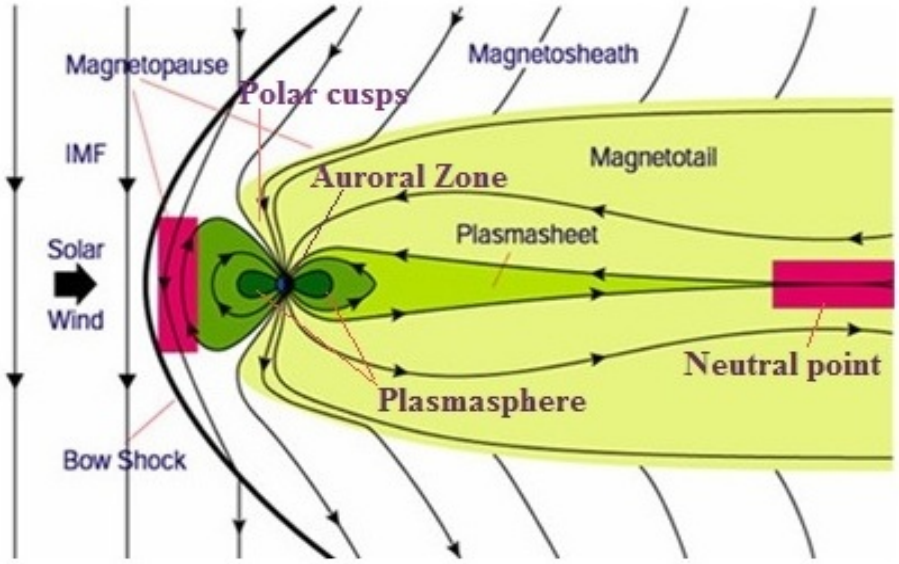

Figure 2.2: The structure of the Earth's Magnetosphere. *Adapted from Singh (2019)*

2.5.2 Solar Wind-Magnetosphere Interaction

Most geomagnetic processes in the magnetosphere and ionosphere depend heavily on the interaction between solar wind and magnetosphere (Pudovkin and Semenov, 1985). This interaction transfers energy and momentum from the solar wind into the magnetosphere.

However, not all solar wind particles enter the magnetosphere because the Earth's geomagnetic field deflects many charged particles (Russell, 2000), shielding Earth from harmful high energy solar particles. Still, some solar wind energy does penetrate, and the amount depends on factors like the direction of the interplanetary magnetic field (IMF) and solar wind density and velocity (Dungey, 1961). The main processes that transfer solar wind energy into the magnetosphere are magnetic reconnection and viscous interaction (Russell, 2000).

Magnetic reconnection

According to Yamada et al. (2010), magnetic reconnection entirely depends on the orientation of the magnetic fields during the interaction of the solar wind with the magnetosphere. Specifically, reconnection happens when the interplanetary magnetic field (IMF) points southward (antiparallel) while the geomagnetic field points northward (Dungey, 1961). If the field lines run parallel, no merging occurs. At the reconnection site, where opposite magnetic polarities meet, the field lines break and reconnect, releasing stored magnetic energy. This energy release accelerates particles and triggers high energy phenomena such as solar flares and geomagnetic storms. During reconnection, geomagnetic pressure redirects the solar wind flow closing the magnetosphere and blocking energy entry (Yamada et al., 2010). Therefore, energy transfer into the magnetosphere is intermittent and fluctuates unpredictably, influenced by solar activity and IMF direction.

Bow shock

The solar wind and the interplanetary magnetic field (IMF) undergo sudden changes in density, temperature, flow speed, and magnetic strength as the fast-moving solar wind approaches the Earth's sun-facing region (Fairfield, 1971). This abrupt shift creates a standing shock wave called the bow shock when the supersonic solar wind meets the Earth's magnetosphere, acting as an obstacle (Fairfield, 1971). Situated approximately 15 Earth radii (RE) from the Sun-Earth line, the bow shock slows the solar wind from supersonic to subsonic speeds, heating and deflecting it (Leroy et al., 1982). The bow shock marks where the solar wind's rapid flow sharply changes as it encounters the magnetosphere, often triggering space weather events like geomagnetic storms (Fairfield, 1971). Because it forms just before these disturbances affect Earth, the bow shock's occurrence time serves as a reliable reference for the start of a geomagnetic storm (Fairfield, 1971). According to Yokoyama and Kamide (1997), the bow shock begins gradually and is usually preceded by a noticeable sudden storm commencement (SSC), signaling the onset of the storm.

2.5.3 Ring current

The ring current is a flow of charged particles, mostly ions, circulating westward around Earth near the equatorial plane at altitudes between 10,000 and 60,000 km (Daglis, 2006; Treumann and Baumjohann, 1997). This current is made up of energetic particles like protons and electrons, which drift due to Earth's magnetic and electric fields, with ions carrying energies from about 10 keV10 keV up to several hundred keV, heavily influencing the current density (Williams, 1985). Electrons contribute little to the ring current because of their low energy. The ring current is closely linked to geomagnetic storms and significantly affects their strength (Treumann and Baumjohann, 1997). During such storms, large amounts of energetic particles enter Earth's inner magnetosphere, boosting the ring current (Daglis et al., 1999). As the ring current grows stronger, it produces a magnetic field opposing Earth's main field, reducing geomagnetic field strength at low and mid-latitudes (Lovell et al., 2020). This weakening shows up as a drop in the Dst index, a key measure of storm severity (Kozyra and Liemohn, 2003). In summary, the intensification of the ring current directly relates to the severity of geomagnetic storms.

2.5.4 Geomagnetic storms

A geomagnetic storm is a significant temporary disturbance in Earth's magnetosphere caused by an enhanced transfer of energy from the solar wind into the space environment around Earth (Gonzalez et al., 1994; Engebretson et al., 2003). This occurs when charged particles from the Sun interact with Earth's magnetic field, compressing the dayside magnetosphere and injecting energy that intensifies currents such as the ring current and auroral electrojets, leading to a global disruption of the magnetic field (Gonzalez et al., 1994). Geomagnetic storms can last from several hours to days (Tsurutani et al., 1992). Their occurrence varies with the solar cycle. The corotating interaction region (CIR) driven storms are more common during solar minimum, while coronal mass ejection (CME) driven storms occur more often during solar maximum (Singh, 2019).

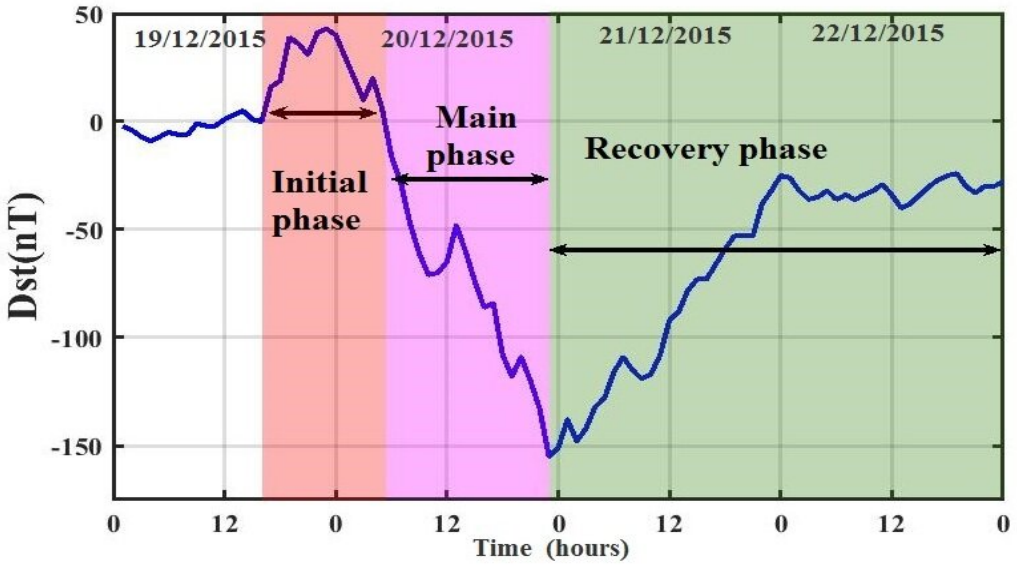

Figure 2.3: Phases of geomagnetic storm (Dst variation, 19^{th}- 22^{nd} Dec 2015.)

Adapted from Singh (2019)

A geomagnetic storm has three phases as indicated in Figure 2.3 they include; the initial, main and recovery phase (Gonzalez et al., 1994). The initial phase is characterised by a sudden increase in of the magnetic field (sudden storm commencement) brought on by interplanetary shock wave compressing the magnetosphere which is then followed by an increase in magnetic field (Engebretson et al., 2003). The initial phase is not always observed and it lasts for until IMF Bz turns southwards. Once the IMF turns to the south, the the main phase of the storm begins which results in a significant drop in the magnetic field's horizontal component (Fairfield, 1971). The recovery phase is attributed to the ring current decay until the total magnetic field returns to the original values. The main phase of storms caused by CMEs is intense and sharp in contrast storms driven by CIRs (Harrison et al., 1990). However, compared to magnetic storms caused by CMEs, CIR-induced storms have longer recovery phases (Hundhausen, 1999). During the period of high solar activity, short-term phenomena like CME driven geomagnetic storms have got a severe impact on the Earth's magnetosphere; conversely, during period of low solar activity, CIR driven storms have got a significant impact. It is believed that these activities are related to periodic occurrence of solar coronal holes in the Sun (Singh, 2019).

A geomagnetic storm that occured between 19th-22nd December 2015 in the Figure 2.3 illustrates the three phases of storm in relation to Dst index. It should be noted that during the geomagnetic storm, the ionospheric disturbance intensifies, this phenomenonon is characterised by irregularities in electron density and TEC with in the ionosphere (Engebretson et al., 2003). The impacts of geomagnetic storms on TEC are complicated and can lead to a rapid and notable variations in TEC values. These variations may

have serious consquencies on systems whose accuracy rely on precise TEC data such as satellite navigation and communication (Pi et al., 2000).

2.5.5 Indices of geomagnetic activity

The global geomagnetic space weather indices such as disturbance storm time (Dst), planetary K (Kp) and solar wind parameter IMF (Bz) are used to quantify and characterise the storm events.

The Disturbance Storm Index (Dst)

The Disturbance Storm Time (Dst) index measures geomagnetic activity and is used to assess the intensity of geomagnetic storms (Sugiura and Iyemori, 2014). It tracks the average variation in Earth's horizontal magnetic field, primarily caused by the ring current flowing around the planet (Sugiura and Iyemori, 2014). Expressed in nanoteslas (nT), the Dst index becomes more negative as storm strength increases (Gonzalez et al., 1994). For example, Matamba and Habarulema (2018) classified storms as severe when $\text{Dst} < -100$ nT, moderate when -100 nT $\leq \text{Dst} < -50$ nT and weak whenever -50 nT $\leq \text{Dst} < -25$ nT. The Dst index provides a quantitative measure of geomagnetic disturbances at low latitudes with a 1-hour resolution (Gonzalez et al., 1994). Negative Dst values indicate ongoing geomagnetic storms, with larger negative values representing stronger storms (Piddington, 1964). The decline in the Dst index links mainly to the intensified ring current flowing westward near the equator (Sugiura and Iyemori, 2014). During strong storms, extreme drops in Dst lead to prompt penetration of ionospheric electric fields in mid-latitude and equatorial regions (Tsurutani et al., 2008).

The planetary K index (Kp)

The Kp index is a widely recognized measure of geomagnetic activity that quantifies disturbances in Earth's magnetic field. It is based on data from a global network of mid-latitude geomagnetic observatories (Menvielle and Berthelier, 1991). The index ranges from 0 to 9, where a value of $\text{Kp} \leq 3$ indicates quiet conditions, and values above 3 signal disturbed geomagnetic conditions (Jurua et al., 2024). The Kp index is calculated every three hours, providing a global overview of geomagnetic activity over time. It reflects the combined impact of solar phenomena such as solar flares, coronal mass ejections (CMEs), and high-speed solar wind streams, all of which affect the magnetosphere (Menvielle and Berthelier, 1991). Due to its broad coverage and frequent updates, the Kp index is extensively used by space weather forecasters and researchers to monitor geomagnetic storms and assess potential impacts on satellites, communication networks, power grids and navigation systems (Singh, 2019).

The IMF Bz index

The IMF is a vector quantity, it consists of three axis components represented as $B = (B_x, B_y, B_z)$. The components B_x and B_y lie within the ecliptic plane while B_z is oriented perpendicular to it. The B_x direction points toward the Sun, z is perpendicular to the ecliptic plane and $y = z \times x$. As noted by Gonzalez et al. (1994), the strength of geomagnetic storms is strongly linked to sustained southward B_z components which enable effective energy transfer from the solar wind into the magnetosphere. This phenomenon is particularly relevant at lower latitudes where such coupling leads to intensified geomagnetic activity. Therefore, the B_z component is the most critical compared to B_x and B_y (Singh, 2019).

2.6 Magnetosphere-Ionosphere Coupling

Magnetosphere-ionosphere coupling is fundamental to dynamics in Earth's near-space environment, especially during geomagnetic storms when solar wind energy and momentum are transferred first to the magnetosphere and then into the ionosphere via field-aligned currents (Frey et al., 2003). Two primary processes regulate equatorial ionospheric electric fields during such storms: Prompt Penetration Electric Fields (PPEFs) and Disturbance Dynamo Electric Fields (DDEFs) (Huang et al., 2016b). PPEFs develop immediately after geomagnetic disturbances, rapidly altering the equatorial ionospheric electric field and enhancing post-sunset plasma irregularities that cause scintillation, as demonstrated in studies by Huang et al. (2016b). DDEF arises from storm-time high-latitude energy inputs that modify global thermospheric circulation, producing longer-lasting changes in the ionospheric electric field. The pre-reversal enhancement (PRE),an evening rise in the zonal electric field is critical in lifting the F-layer to altitudes conducive to plasma instability and scintillation (Huang et al., 2016b). East Africa is especially vulnerable due to an intense PRE and a pronounced equatorial ionization anomaly (EIA), both of which amplify ionospheric irregularities (Frey et al., 2003). Importantly, the timing of geomagnetic storm onset, marked by the southward turning of the IMF Bz (bow shock time), determines the strength and timing of PPEF and PRE effects in the equatorial ionosphere. This temporal relationship underpins the present study's focus on storm commencement time as a key driver of scintillation activity and GNSS disruption in East Africa.

2.6.1 Prompt Penetration Electric Fields

Prompt Penetration Electric Fields (PPEFs) appear almost immediately in response to sudden changes in the interplanetary magnetic field (IMF) and the interaction between the solar wind and magnetosphere during geomagnetic storms. They quickly carry electric fields from the magnetosphere down to the equatorial ionosphere with very little delay. PPEFs disrupt the usual electric field patterns by either strengthening or reversing the normal eastward electric fields, impacting plasma drifts and densities on both the day

and night sides (Frey et al., 2003). These fields typically last about 1 to 2 hours and are directed eastward during the day and westward at night, playing a key role in disturbing ionospheric conditions during the early stages of geomagnetic storms (Huang et al., 2016b; Kikuchi et al., 2008).

2.6.2 Disturbance Dynamo Electric Field

Disturbance Dynamo Electric Fields (DDEF) are produced as a delayed, secondary response to geomagnetic storms. They arise from changes in thermospheric winds, which generate electric currents and create disturbance dynamo fields that usually appear hours after storm onset and last longer. DDEF effects are most prominent at low and mid-latitudes, with a slower impact on the ionosphere compared to Prompt Penetration Electric Fields (PPEFs) (Fejer et al., 2008b; Dugassa et al., 2019). The zonal component of DDEF points westward during the day and eastward at night, opposite to the typical day/night ionospheric dynamo fields. Distinguishing the effects of PPEF and DDEF during storms is challenging, as their generation mechanisms are understood, but separating their contributions is difficult (Maruyama et al., 2005).

2.6.3 Pre reversal Enhancement

The pre-reversal enhancement (PRE) is a boost in the eastward electric field that happens just before it switches to westward around sunset in the equatorial ionosphere (Rishbeth, 1971). This phenomenon is crucial for understanding how the ionosphere behaves and how irregularities develop, especially in low-latitude areas. PRE usually occurs between sunset and midnight and is marked by a surge in the eastward electric field, which causes stronger upward drifts of ionospheric plasma (Abdu, 2005). This increase is mainly driven by changes in thermospheric wind patterns and the electromagnetic link between the ionosphere and magnetosphere. During geomagnetic storms, PPEFs can amplify the PRE, pushing plasma drifts beyond usual levels and leading to plasma bubbles and irregularities that can disturb GNSS signals (Maruyama et al., 2005).

2.7 Ionospheric Irregularities and Instabilities

2.7.1 Rayleigh-Taylor Instability

The ionosphere experiences critical electrodynamic and structural transformations following sunset due to the cessation of solar radiation, although ionized plasma, especially in the F-layer, temporarily persists and is elevated by intensified eastward electric fields (Kull, 1991). As the F-layer ascends through the $E \times B$ drift, the base thins, generating a steep electron density gradient that forms an interface with denser plasma situated above lighter plasma. This creates an unstable equilibrium known as the Rayleigh-Taylor Instability (RTI), occurring when a heavier fluid overlies a lighter one under gravity

(Kull, 1991). Over time, small disturbances at this interface amplify, causing denser plasma to descend and lighter plasma to ascend, producing plasma "bubbles" the regions of significantly depleted electron density (Kelley, 2009b). These plasma bubbles typically form during post-sunset hours, are intensified during geomagnetic storm periods when the F-layer is uplifted by strong eastward electric fields (Abdu, 2005; Wu et al., 2019), and extend to higher altitudes while persisting for hours in low-latitude regions like East Africa (Praveena et al., 2020). These irregularities are the primary source of small-scale plasma disturbances causing rapid fluctuations and scintillation in GNSS signals within the critical post-sunset interval (Wu et al., 2019). Consequently, plasma bubbles constitute a prominent space weather factor affecting communication, navigation, and timing systems in equatorial regions, with geomagnetic storms exacerbating the plasma uplift and RTI-driven instability development (Abdu, 2005).

2.8 Global Navigation Satellite System

Global Navigation Satellite Systems (GNSS) refer to satellite-based networks that provide worldwide positioning, navigation, and timing services (Kintner et al., 2007b). Prominent GNSS constellations include the American Global Positioning System (GPS), Russian GLONASS, European Galileo, and Chinese BeiDou (Hofmann-Wellenhof et al., 2007). These systems transmit signals on multiple frequencies such as L1, L2, and L5, which GNSS receivers process to determine precise user locations (Kintner et al., 2007b). GPS, initially developed for military purposes but now widely available for civilian use, is the most extensively utilized GNSS worldwide. It comprises 32 medium Earth orbit satellites supported by ground-based control stations that synchronize satellite clocks and monitor functionality (Ali et al., 2020; Misra and Enge, 2006). GPS receivers, categorized into single- and dual-frequency types, decode signals from satellites; dual-frequency receivers offer improved accuracy by tracking both L1 and L2 frequencies, whereas single-frequency receivers track only L1 and are less precise but more affordable (Kintner et al., 2007b). Despite GNSS's widespread utility, these systems are vulnerable to degradation from space weather phenomena, particularly ionospheric Total Electron Content (TEC) variations and scintillation (Hofmann-Wellenhof et al., 2007). Ionospheric disturbances cause signal delays, phase and amplitude scintillations, loss of lock, and positioning errors, critically impacting GNSS accuracy and reliability (Kintner et al., 2007b). This vulnerability is especially pronounced in equatorial regions such as East Africa, where the Equatorial Ionization Anomaly (EIA) and frequent post-sunset plasma bubbles cause intense scintillation events (Ali et al., 2020). Studies have documented consistently higher scintillation rates and greater positional errors in this region compared to mid-latitudes, highlighting the urgent need for targeted research and mitigation (Ali et al., 2020).Therefore, understanding and predicting ionospheric influences on GNSS signals in low-latitude East Africa is critical for enhancing navigation system reliability in this

region, where dependence on GNSS spans aviation, telecommunications, transportation, and emergency response systems.

2.9 Propagation of radio waves through the ionosphere

Radio wave propagation through the ionosphere is significantly influenced by free electrons, which cause refraction and signal delay proportional to the total electron content (TEC) along the propagation path (Budden, 1985; Waters and Cox, 2009). For radio waves to penetrate the ionosphere effectively, their frequency must exceed the ionosphere's critical frequency, including the X-mode and O-mode cutoffs ranging from a few to tens of MHz (Davies, 1990). GNSS signals operate at frequencies well above these thresholds, allowing them to pass through the ionosphere with minimal alteration under uniform conditions (Kintner et al., 2007b). However, ionospheric inhomogeneities, particularly prevalent at low latitudes like East Africa, introduce complex effects such as reflection, refraction, and diffraction due to fluctuations in electron density and refractive index (Aarons, 1982; Budden, 1985). Large-scale ionospheric effects primarily cause signal delay and refraction, which are generally modeled and corrected in GNSS positioning (Kintner et al., 2007b). In contrast, small-scale irregularities induce ionospheric scintillation in form of rapid amplitude and phase fluctuations that can cause signal fading, loss of lock, and positioning errors, posing significant challenges to GNSS reliability (Singh, 2019). Scintillation events are particularly intense and frequent in equatorial regions due to post-sunset plasma bubble activity, which disrupts the ionospheric electron density (Kintner et al., 2007b). In East Africa, strong scintillation during post-sunset periods degrades navigation and communication system performance, underscoring the critical need to understand and model these propagation effects for regional GNSS applications (Kintner et al., 2007b). The detailed understanding of how the ionosphere affects radio waves distinguishing between large-scale signal delays and small-scale signal fluctuations (scintillation) shows why this study focuses on ionospheric irregularities. These irregularities significantly impact the accuracy and reliability of GNSS signals, especially in low-latitude regions like East Africa where such disturbances are most severe. This focus is essential for improving GNSS performance and addressing challenges unique to this area.

2.10 Ionospheric scintillation

Ionospheric scintillation is the rapid fluctuation in radio signal amplitude and phase caused by plasma irregularities in the ionosphere (Kintner et al., 2007b). These fluctuations degrade signal quality and can cause GPS receivers to lose lock, increasing navigation errors or failures (Aarons, 1982; Basu et al., 2002a). Scintillation arises from refractive and diffractive effects as radio waves traverse irregular plasma densities,

causing signal phase interference (Kintner et al., 2007b). Globally, scintillation is most intense at high and low latitudes, with the equatorial region especially East Africa being one of the strongest scintillation belts due to plasma bubbles linked to the equatorial ionization anomaly (EIA) during post-sunset (Conker et al., 2000). These irregularities cause amplitude scintillation, signal fading, cycle slips, and loss of lock, which are harder to predict than large-scale ionospheric delays (Kintner et al., 2007b). A related factor that can mimic or exacerbate scintillation effects is multipath, where signals reflect off nearby surfaces before reaching the receiver antenna, producing interference patterns that resemble ionospheric scintillation (Braasch, 1996). Multipath effects depend on the local environment, receiver antenna design, and satellite geometry, complicating signal interpretation and error correction (Conker et al., 2000). Research mainly focuses on storm intensity impacts, but scintillation does not always align with storm strength. Instead, storm onset timing and particularly the southward turning of IMF Bz which governs the occurrence of prompt penetration electric fields and pre-reversal enhancements that drive scintillation onset and severity in the equatorial ionosphere (Singh, 2019). This timing relationship is central to understanding regional scintillation variability in East Africa. Moreover, slower plasma drift velocities and longer plasma irregularities at low latitudes cause amplitude scintillation to dominate the East African region (Abiriga et al., 2021). Frequent scintillation and multipath combined strain GPS receivers operating at fixed frequencies, reducing recovery time after cycle slips or loss of lock, thus elevating navigation errors during intense ionospheric disturbance periods (Basu et al., 2002a). Generally, the complex interplay of ionospheric irregularities, storm timing, and multipath effects critically influences GNSS performance in East Africa, underscoring the need for regionalized models and mitigation strategies.

2.10.1 Amplitude scintillation

Amplitude scintillation is the rapid fluctuations in the strength/amplitude of signals as they propagate through the ionosphere (Kintner et al., 2007b). These fluctuations result from irregularities in the ionosphere specifically due to variations in electron density (Basu et al., 2002b). Amplitude scintillations predominantly occurs at low latitudes during the post sunset hours. This dominance is attributed to the unique behavior of radio signal propagation in the low-latitude region. This is brought particularly by the distinct electrodynamic characteristics of the ionosphere in this region. It should be noted that in the lower latitude region, plasma drift velocities are generally lower compared to those at higher latitudes. This slower movement results in the formation of larger scale plasma irregularities (Abiriga et al., 2021). These larger irregularities tend to have a more significant impact on the amplitude of radio signals in low latitude areas. The fluctuations in signal strength caused by this effect are known as amplitude scintillation. Amplitude scintillation is quantified using the scintillation index S4 as measured by GPS

receivers (Abiriga et al., 2021; Kintner et al., 2007b). Conversely, at high latitudes, plasma irregularities are smaller in scale and occur at higher drift velocities. This leads to rapid changes in signal phase, resulting in phase scintillation rather than amplitude scintillation (Spogli et al., 2009). Therefore, the dominance of amplitude scintillation in low latitude regions stems from their unique ionospheric and electrodynamic properties, distinguishing them from high latitude areas where phase scintillation is more prevalent (Aarons, 1997).

Amplitude scintillation occurs more frequently after sunset (Kelley, 2009b). This is due to the fact that after sunset, rapid recombination of ionospheric plasma in the lower altitudes creates steep vertical gradients in electron density. This leads to Rayleigh-Taylor instability, causing "bubbles" of low-density plasma to rise from lower to higher altitudes (Basu et al., 2002b). As these bubbles ascend, they create turbulence and irregularities in electron density along their path, causing GPS and other radio signals passing through them to scintillate. Amplitude scintillation effects are severe for Very High Frequency (VHF) signals compared to Ultra High Frequency (UHF) signals (Praveena et al., 2020).

The S4 index is primarily determined by a normalized standard deviation of signal intensity recorded over a specific time interval. This signal intensity is expressed in terms of Signal to Noise Ratio (SNR) (Datta-Barua et al., 2003; Guo et al., 2019). A higher SNR signifies a stronger and clearer signal compared to the noise, whereas a lower SNR represents a weaker signal that is harder to distinguish from the noise (Tandra and Sahai, 2008). Amplitude scintillation is described by the scintillation index S4 and it refers to the standard deviation of the received signal power measured at a rate of 50 samples per second, normalized by its mean value (Abiriga et al., 2021). Amplitude scintillation S4 is mathematically expressed in the equation 2.1

$$\mathrm{S4} = \sqrt{\frac{\langle \mathrm{I}^2 \rangle - \langle \mathrm{I} \rangle^2}{\langle \mathrm{I} \rangle^2}} \tag{2.1}$$

I is the mean incoming signal power in Watts (W) and S4 is the amplitude scintillation index (Abiriga et al., 2021). When amplitude scintillation becomes intense, the SNR of the GPS receiver decreases. This reduction weakens the received signal and can push it below the lock threshold. As a result, errors occur in GPS carrier measurements. This condition leads to a loss of code lock on the GPS signal. (Salles et al., 2021). The lock threshold is determined by the bandwidth of the GPS receiver system. It is also influenced by the tracking channel of the receiver. The SNR can be mathematically expressed in the equation 2.2

$$\frac{\mathrm{S}}{\mathrm{N}} = \frac{P_{\mathrm{signal}}}{P_{\mathrm{noise}}} = \left(\frac{A_{\mathrm{signal}}}{A_{\mathrm{noise}}} \right)^2 \tag{2.2}$$

P is the average power in W and A is the root mean square amplitude in volts (V). SNR is usually expressed in decibels (dB) given by the equation 2.3

$$\frac{\mathrm{S}}{\mathrm{N}}(\mathrm{dB}) = 10\log_{10}\frac{P_{\mathrm{signal}}}{P_{\mathrm{noise}}} = 20\log_{10}\left(\frac{A_{\mathrm{signal}}}{A_{\mathrm{noise}}}\right) \tag{2.3}$$

The Carrier to Noise Ratio (CNR) is the SNR of a processed signal. A higher CNR value means better reception quality. It is expressed in dB/Hz and mathematically defined by the equation 2.4

$$\frac{\mathrm{C}}{N_0} = \frac{\mathrm{C}}{K_{\mathrm{B}}T} \tag{2.4}$$

The received carrier power is denoted as C in watts, K_{B} represents Boltzmann's constant in Joules per Kelvin, and T is the receiver system noise temperature measured in Kelvin (K). According to Dubey et al. (2005), the nominal carrier-to-noise ratio (CNR) for the L1 band is 45 dB/Hz. Signal tracking is interrupted when the CNR falls below 24 24 dB/Hz. The study also notes that the L2 signal is more vulnerable to decreases in CNR compared to L1, mainly because the L2 power 6 dB lower than that of L1.

Basing on the S4 values, scintillation events are categorised as weak, moderate and strong. An event is considered weak when $0.2 < \mathrm{S4} \leq 0.4$, moderate when $0.4 < \mathrm{S4} \leq 0.6$ and strong when $0.6 < \mathrm{S4} \leq 1.2$ according to the study by Jurua et al. (2024). In the same study the lower and upper threshold values of S4 were set at 0.2 and 1.2 respectively. All the S4 values that lied below 0.2 were considered as background noise.

2.10.2 Phase scintillation

Phase scintillation is a rapid fluctuation in the phase of a radio signal as it passes through the ionosphere (Basu et al., 1998). These fluctuations result from small-scale irregularities in ionospheric electron density, which create random variations in the path length and velocity of the signal as it travels to the receiver (Yeh and Liu, 1982). These irregularities introduce rapid, random phase shifts, causing the signal's phase to vary unpredictably over time. In GPS and satellite communications, phase scintillation can lead to errors in phase-based measurements which impacts the accuracy of systems that rely on precise timing and positioning. This effect is particularly concerning GPS applications where phase information is critical for calculating accurate positions (Kintner et al., 2007b). Phase scintillation tends to be most intense in polar and equatorial regions especially during periods of high geomagnetic activity when ionospheric disturbances are more pronounced (Aarons, 1997). These ionospheric disturbances at the poles enhance ionospheric turbulence leading to increased irregularities in electron density. As signals pass through disturbed ionospheric regions, they experience larger variations in path length and speed,

leading to stronger phase fluctuations (Gulyaeva, 2003). In contrast, low-latitude areas near the equator face unique ionospheric behaviors, such as the formation of equatorial plasma bubbles, which mainly affect amplitude scintillation instead of phase (Basu et al., 1998). Phase scintillation is measured using carrier-phase data, and its intensity is quantified by the phase scintillation index σ_ϕ , defined as the standard deviation of the carrier-phase measurements, mathematically expressed in equation 2.5 (Demyanov et al., 2019).

$$\sigma_\phi = \sqrt{\langle \phi^2 \rangle - \langle \phi \rangle^2} \tag{2.5}$$

where ϕ is the signal phase in degrees or radians. Rapid changes in signal frequency caused by phase scintillation can cause GPS receivers to lose signal lock. When the Doppler shift exceeds the bandwidth of the phase lock loop (PLL), the receiver fails to maintain phase lock due to errors in the apparent range rate (Van Dierendonck et al., 1993).

Chapter 3

Data and Methods

This chapter describes the data, data sources used in this study and the procedures adopted to process it to achieve a set of objectives. Section 3.1 describes the sources of data used, section 3.2 gives details on data analysis and processing while section 3.3 explains the methods used to achieve each objective.

3.1 Data sources

3.1.1 Geomagnetic Storm Data

The Geomagnetic Storm Data were sourced from NASA's OMNIWeb data explorer (`http://omnweb.gsfc.nasa.gov/form/dx1.html`) for the period 2011 to 2016 and include three primary geomagnetic indices: Dst, Kp, and IMF Bz. The datasets have varying temporal resolutions, typically with Dst reported on an hourly basis, Kp on three hourly basis while IMF Bz data are available at finer resolution of 1-minute intervals (Gonzalez et al., 1994).The Disturbance Storm Time (Dst) index was selected for storm intensity classification due to its sensitivity to the ring current and global geomagnetic storm magnitude. The Kp index, representing global geomagnetic activity derived from ground magnetometer measurements, was included to assess overall auroral and substorm activity levels (Bartels et al., 1939). IMF Bz, the north-south component of the interplanetary magnetic field, was critical for determining storm onset timing, as its sustained southward orientation facilitates magnetic reconnection and energy transfer into Earth's magnetosphere (Dungey, 1961).

3.1.2 Ionospheric Scintillation Data

The ionospheric scintillation data used in this study were obtained from two SCINDA GPS receiver stations located at Makerere University (MAK) and Mbarara University of Science and Technology (MBA).The geographical location of these receivers are indicated in the Figure 3.1 and their coordinates listed in Table 3.1.

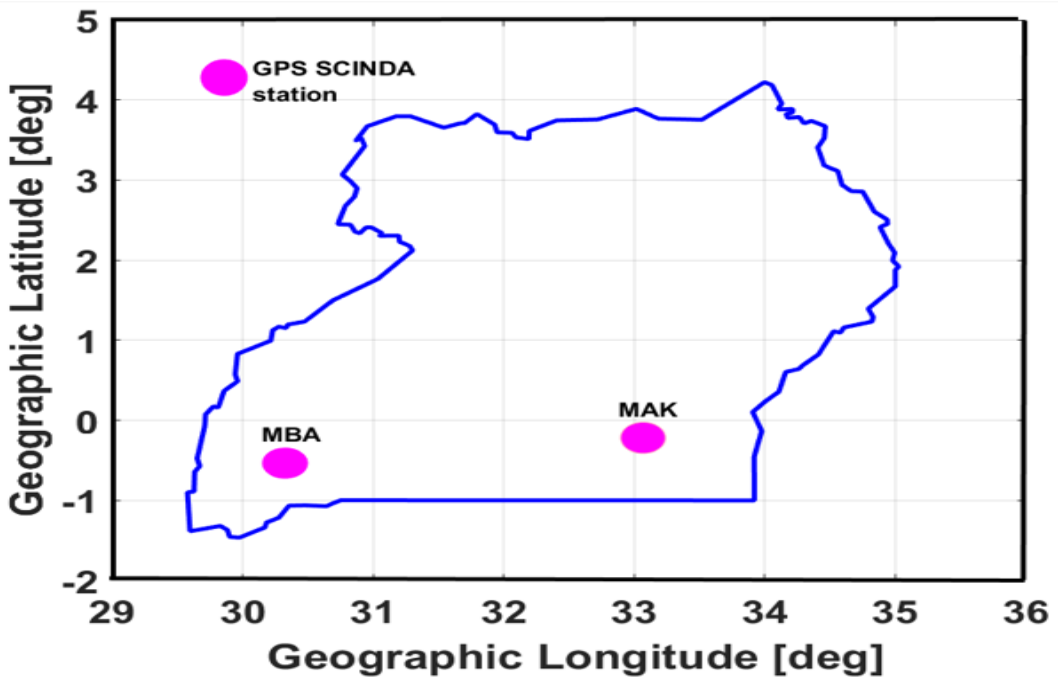

Figure 3.1: Map of Uganda showing SCINDA receiver stations (Mbarara, Makerere)

Table 3.1: Locations GPS SCINDA receivers used in this study

Station			Geographic		Geomagnetic	
Place	Type	Code	Lon (^{o}E)	Lat (^{o}N)	Lon (^{o}E)	Lat (^{o}N)
Makerere	GPS-SCINDA	MAK	32.57	0.35	104.2	-9.3
Mbarara	GPS-SCINDA	MBA	30.66	-0.62	108.5	-11.03

These data cover the period from 2011 to 2016, closely matching the geomagnetic storm period under study. The SCINDA system records scintillation at a 1-minute resolution derived from raw data sampled at higher rates (Groves et al., 1997). The key scintillation parameter analyzed is the amplitude scintillation index, S4, where values above 0.2 typically indicate meaningful scintillation events (Groves et al., 1997). The data are stored in SCN and PCN file formats and include continuous measurements of signal amplitude and phase fluctuations. Figure 3.2 illustrates the monthly availability of valid data days, highlighting gaps resulting from receiver malfunctions and maintenance issues. These interruptions reflect challenges in ground-based ionospheric monitoring but

still allow robust analysis due to substantial data coverage (Bartels et al., 1939). This figure shows the number of days with scintillation data for each month of the years under study.

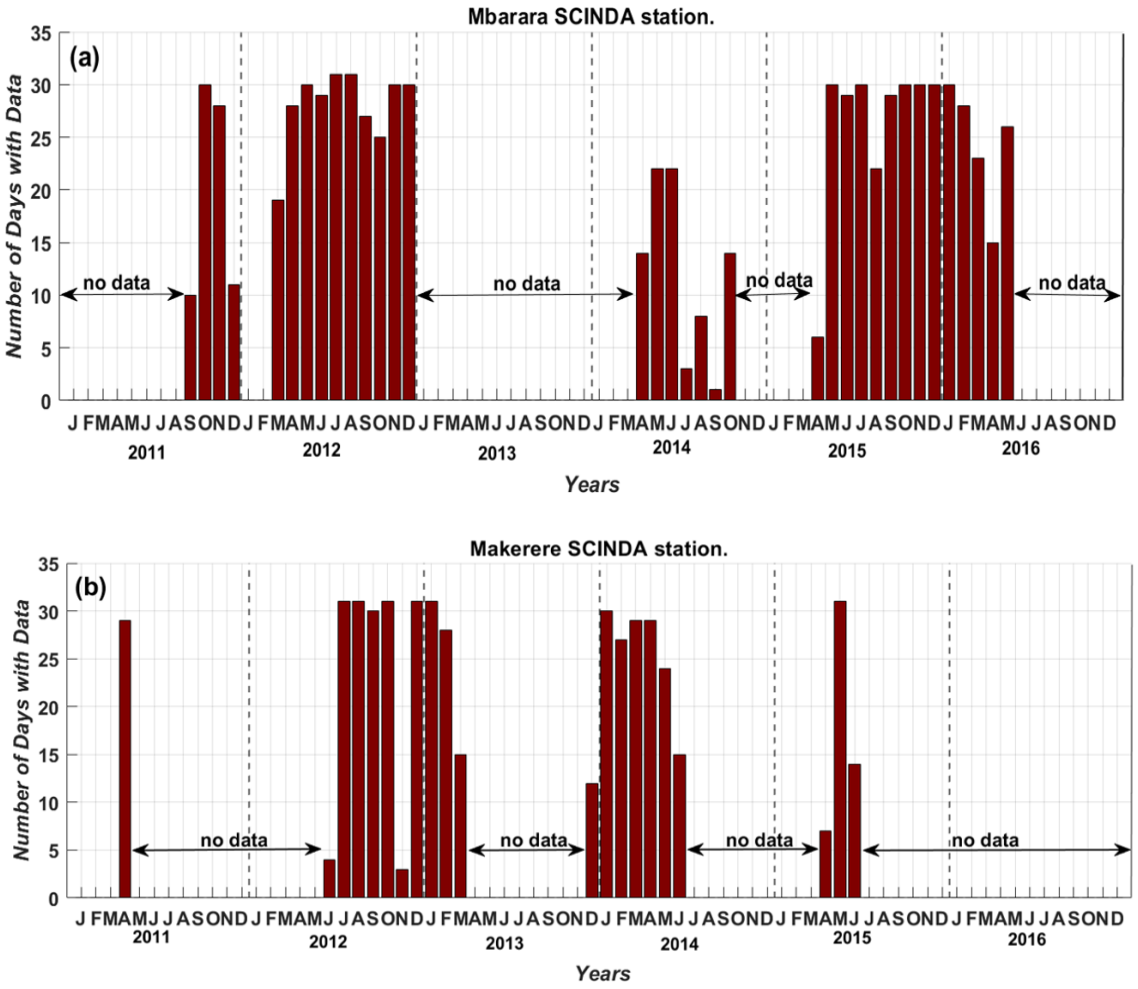

Figure 3.2: Number of days with valid scintillation data (2011-2016)

3.2 Data Processing

The raw scintillation data used in this study were obtained from SCINDA GPS receivers at Makerere University (MAK) and Mbarara University of Science and Technology (MBA). These data, recorded in SCN and PCN file formats, were processed using the GPS-TEC software developed by Gopi Seemala (Seemala and Valladares, 2008). This program converts raw scintillation data into 10-column CMN files containing Julian date, measurement time, satellite number designated by the Pseudo-Random Noise (PRN) code, satellite azimuth and elevation angles, ionospheric pierce point coordinates, slant TEC, vertical TEC, and amplitude scintillation index (S4). To enhance data quality, only measurements from satellites with elevation angles greater than 30° were considered, which helps reduce multipath effects (Amabayo et al.,(2014)). Outliers likely caused by instrument errors were removed by excluding S4 values exceeding the theoretical

maximum of $\sqrt{2}$(Hlubek et al., 2014). Additionally, scintillation events were defined as those with S4 values exceeding a lower threshold of 0.2, considered the background noise level (Jiao and Morton, 2015). The processed data were aggregated into monthly datasets with percentage occurrences calculated for weak ($0.2 < S4 \leq 0.4$), moderate ($0.4 < S4 \leq 0.6$), and strong ($S4 > 0.6$) scintillation events (Jurua et al., 2024). These processing steps align with standard SCINDA usage best practices and ensure robust representation of scintillation climatology over the study period.

3.3 Methods

3.3.1 Geomagnetic Storm Classification

Geomagnetic storms were characterized into three phases: initial, main, and recovery. Storm onset was determined by the bow shock arrival time, identified as the epoch when IMF Bz first transitions to a sustained southward orientation (Dungey, 1961). The Dst index was used to classify storm intensity into weak ($-50nT \leq Dst < -25nT$), moderate ($-100nT \leq Dst < -50nT$), and severe ($Dst < -100nT$) categories, following Matamba and Habarulema (2018), with justification for deviation from standard Gonzalez et al. (1994) thresholds to reflect regional characteristics. The Dst index threshold for weak geomagnetic storms is set differently from the standard Gonzalez et al. (1994) classification, adopting the range $-50nT \leq Dst < -25nT$ as proposed by Matamba and Habarulema (2018). This adjustment reflects the need to better capture region-specific geomagnetic responses, particularly in equatorial and low-latitude areas, where even moderate Dst depressions below -25 nT can significantly affect ionospheric and magnetospheric conditions. Such tailored thresholds enhance the sensitivity of storm impact assessments relevant to the local geophysical environment, thus improving the accuracy and applicability of the results over relying solely on broader global criteria. The Kp index classified geomagnetically quiet days ($Kp \leq 3$) versus storm-disturbed days ($Kp > 3$) (Jurua et al., 2024), with Kp guiding broader identification of activity levels and Dst refining storm strength on identified storm days. Storms were further categorized as CME- or CIR-driven, with weaker/moderate storms attributed to CIR events due to their slower energy input and CME-driven storms validated via the CDAW CME catalog `https://cdaw.gsfc.nasa.gov/CME_list/` (Pandya et al., 2019). Most weak and moderate geomagnetic storms are associated with corotating interaction regions (CIRs), while severe storms are predominantly driven by coronal mass ejections (CMEs) (Pandya et al., 2019). CIRs, caused by the interaction of fast and slow solar wind streams, produce recurrent but generally less intense disturbances, whereas CMEs are large, sudden eruptions from the Sun that inject significant energy into the magnetosphere, leading to stronger geomagnetic storms. This distinction is important because it reflects the different solar wind structures responsible for storms of varying intensity,

allowing for more accurate classification and understanding of storm impacts in space weather studies.

3.3.2 Scintillation Data Analysis

To study ionospheric scintillation morphology and climatology, amplitude scintillation (S4) values from SCINDA receivers were analyzed. S4 values were averaged over 1-minute intervals and only data from satellites with elevation angles 30° were included to mitigate multipath. Scintillation event start/end times correspond to S4 exceeding/dropping below 0.2 threshold (Jiao and Morton, 2015). Events were classified as weak ($0.2 < S4 \leq 0.4$), moderate ($0.4 < S4 \leq 0.6$), and strong ($S4 > 0.6$) (Jurua et al., 2024). Monthly percentages of these categories were calculated using formulas (3.1), (3.2), and (3.3).

$$P_{\text{Weak}} = \frac{N(0.2 < S_4 \leq 0.4) \times 100}{N(S_4 > 0.2)} \tag{3.1}$$

$$P_{\text{Moderate}} = \frac{N(0.4 < S_4 \leq 0.6) \times 100}{N(S_4 > 0.2)} \tag{3.2}$$

$$P_{\text{Strong}} = \frac{N(0.6 < S_4 \leq 1.2) \times 100}{N(S_4 > 0.2)} \tag{3.3}$$

Where N denotes the number of events in the specified S4 range.

3.3.3 Correlation between Geomagnetic Storms and Scintillation

To assess storm onset effects on scintillation, bow shock times were matched with mean S4 values over five-day windows spanning storm onset, peak, and recovery phases (Kintner et al., 2007a). S4 data were averaged over 5-minute intervals using signals from satellites above 30° elevation. Thresholds for average S4 were adjusted:$S4 < 0.1$ (no scintillation), $0.1 < S4 \leq 0.3$ (weak), $S4 > 0.3$ (strong) to account for averaging effects. Lowering S4 thresholds after averaging practically smooths out short-duration peaks in scintillation, reducing the observed index values. The specific values of 0.1 and 0.3 were adapted in this study to compensate for this effect and better align with the true occurrence of ionospheric irregularities. This method enables focused analysis of storm-driven scintillation, minimizing unrelated background disturbances.

Chapter 4

Results and Discussions

This chapter presents the results of the research. The key observations and findings of the study are also discussed.

4.1 Geomagnetic Storms.

This section presents the morphology, the classification and the statistics of geomagnetic storms. The total number of storms in the period between 2011 and 2016 and the number of storms in each category as classified by Matamba and Habarulema (2018) are indicated.

4.1.1 Classification results of geomagnetic storms

The Figures 4.1, 4.2, and 4.3 show intense, moderate, and weak geomagnetic storms from the study. Each plot presents the IMF Bz component (green), Kp index (red), and Dst index (magenta) over several days against Universal Time. A vertical brown dotted line marks the storm onset, aligned with the sharpest southward Bz turning. This southward Bz is critical as it enables magnetic reconnection between the solar wind and Earth's magnetosphere. This process allows energy transfer into the magnetosphere, triggering the geomagnetic storm at the bow shock time.

Figure 4.1 shows two panels (a) and (b) of progressive intense geomagnetic storms. Panel (a) shows a storm that occurred between 15 to 19 March, 2015, and in panel (b) the storm event occurred between 24 to 28 October, 2015.

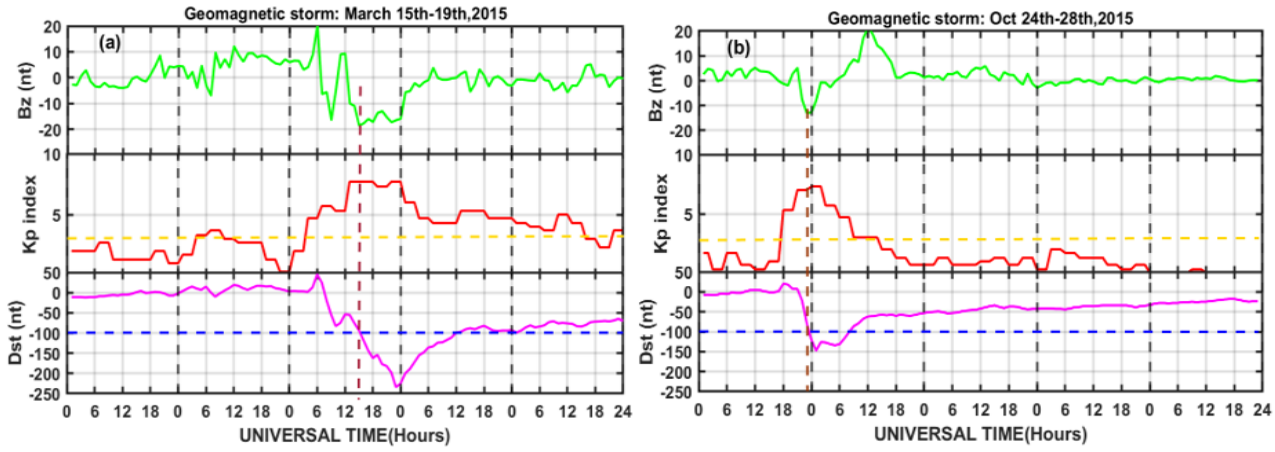

Figure 4.1: Classification of intense geomagnetic storm events ($Dst \leq -100\ nT$)

In panel (a), the storm begun on March 17th, 2015, at around 15:00 UT, marked by a significant southward orientation in the Bz component, reaching -20 nT as indicated by a brown vertical dotted line. The Kp index quickly rose above the yellow horizontal line

drawn at Kp=3, signifying a geomagnetically disturbed day. The Kp index maintained values above this threshold for an extended duration, reflecting the storm's intensity. Correspondingly, the Dst index shows a sharp decline, dropping below -100 nT marked by a blue dotted horizontal line and reached a minimum of around -220 nT, classifying this as a severe geomagnetic storm as categorised by Matamba and Habarulema (2018). According to Gonzalez et al. (1994) this pronounced drop indicates a substantial enhancement of the ring current, driven by strong solar wind magnetosphere coupling. Panel (b) similarly displays the development of an severe storm starting on October 24th, 2015, with the storm commencement time around 23:00 UT, corresponding to a steep southward turning of the IMF Bz as indicated by a brown vertical dotted line. The Bz dropped sharply to about -15 nT, to initiate geomagnetic activity. Shortly after this drop, the Kp index rose significantly above the Kp=3 threshold marked by horizontal yellow dotted line, confirming the day as storm disturbed. The Dst index then fell steeply below the horizontal dotted blue line, reaching a minimum of approximately -149 nT, placing this event in the severe storm category. Although the storm in October 2015 was not as severe as the March 2015 event in terms of Dst depth, it still indicated a powerful enhancement of geomagnetic activity. In both cases, the severe geomagnetic storms followed a consistent sequence; a sudden southward excursion of the IMF Bz, a rapid increase in the Kp index indicating widespread disturbance and a steep drop in the Dst index below -100 nT, confirming the storm's severity. These patterns highlight the strong influence of interplanetary conditions particularly the orientation of the Bz component on the Earth's geomagnetic environment.

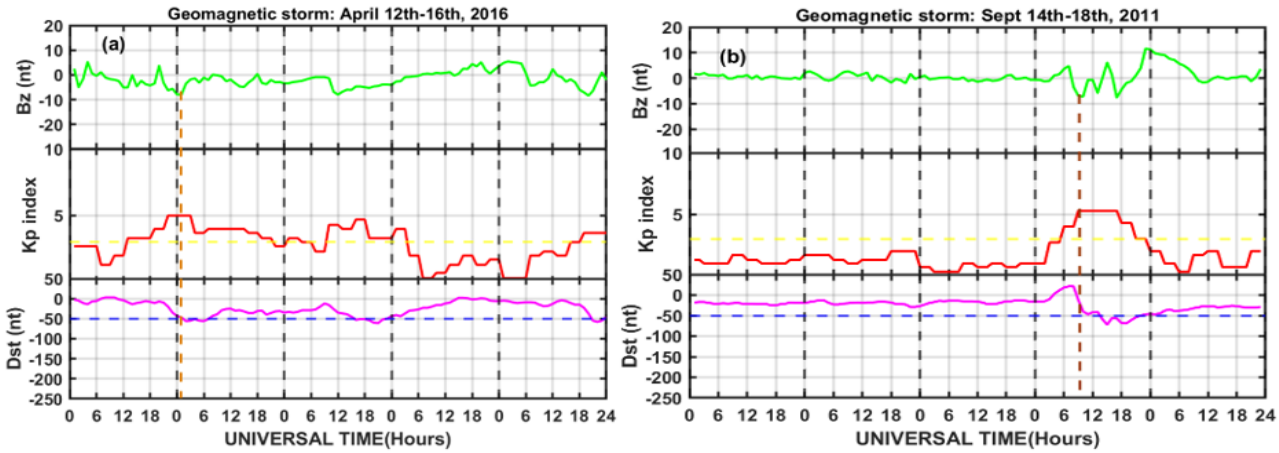

Figure 4.2: Classification of moderate geomagnetic storms ($-100 < Dst \leq -50\ nT$)

The two panels (a) and (b) illustrate the progression of moderate geomagnetic storms. In panel (a), the April 2016 storm begun at around 11:00 UT on April 13th, marked by a distinct decrease in the Bz component to approximately -10 nT as indicated by a brown vertical dotted line. This was followed by a rise in the Kp index to values above 3, indicating a geomagnetically disturbed day. The Kp curve remained above

the horizontal yellow dotted line for a considerable duration, confirming the presence of active geomagnetic conditions. Shortly thereafter, the Dst index droped below -50 nT marked by a blue horizontal dotted line and reached a minimum of approximately -65 nT, which falls within the range of a moderate geomagnetic storm as categorised by Matamba and Habarulema (2018). The Dst curve then exhibited a gradual recovery pattern, typical of moderate storm events. Panel (b) displays a similar pattern during the storm from September 14th to 18th, 2011. The storm onset occured at around 09:00 UT on September 17th, corresponding to a sharp southward turn in Bz to nearly -12 nT. This turning point again led to a rise in the Kp index beyond the threshold of 3, signifying heightened geomagnetic activity. The Dst index also responded with a drop below -50 nT marked by a blue horizontal dotted line, reaching a minimum near -75 nT. As in panel (a), the Dst profile revealed a clearly defined main phase followed by a recovery phase, consistent with the dynamics of a moderate geomagnetic storm. Both panels demonstrated key features associated with moderate geomagnetic storms: the initiation by a southward IMF Bz turning, an accompanying rise in the Kp index beyond 3, and a drop in the Dst index to between -50 and -100 nT. These elements collectively confirm the storms' classification by Matamba and Habarulema (2018) as moderate geomagnetic storms.

Moderate geomagnetic storms occur when the Earth's magnetic field is moderately disturbed by enhanced solar activity such as high-speed solar wind streams from coronal holes (Tsurutani et al., 1992). These storms are less intense than intense storms but still significant with Dst index values ranging between -50 nT and -100 nT. They are not as disruptive as severe storms but still have got notable impacts on both the ionosphere and the magnetosphere (Kappenman, 2005). It should be noted that moderate geomagnetic storms often occur due to CIRs from solar wind streams or small-to-moderate CMEs. CIRs arise from the interaction between fast and slow solar wind streams and are more common during the declining phase of the solar cycle (Borovsky and Denton, 2006). CIR-driven moderate storms are often less abrupt than CME-driven events though they can last longer resulting in sustained geomagnetic disturbances over several days (Kappenman, 2005). Figure 4.3 presents two panels (a) and (b) of typical weak geomagnetic storms.

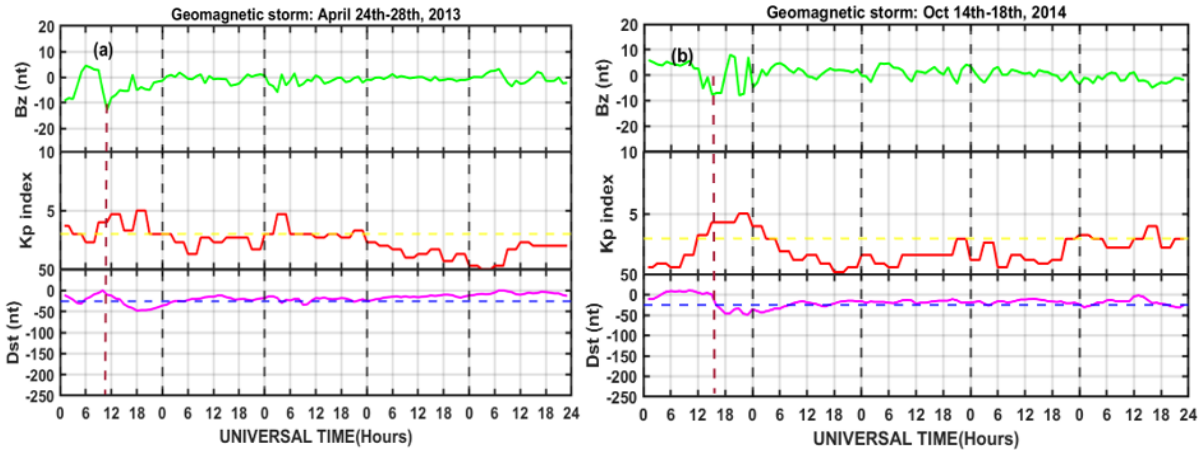

Figure 4.3: Classification of weak geomagnetic storms ($-50 \leq Dst < -25\ nT$)

In panel (a), the storm onset occured at around 11:00 UT on April 24th, 2013, where the IMF Bz reached its peak minimum value as indicated by a brown vertical dotted line. This was immediately followed by a rise in the Kp index, which crossed the yellow horizontal line at Kp=3, indicating that the day was geomagnetically disturbed. The Kp index fluctuated above this threshold for several hours, confirming the storm's active phase. The Dst index, which reflects the intensity of the storm, dropped below -25 nT (below a blue horizontal dotted line) but remained close to -50 nT, categorizing the event as a weak geomagnetic storm. The Dst depression was mild and exhibited a shallow recovery, indicating limited ring current intensification during the event. Similarly, panel (b) showed the October 2014 storm with its onset around 15:00 UT on October 14th, again marked by a clear southward excursion of the IMF Bz component and indicated by a brown vertical horizontal line. The Kp index, in response, rose above the Kp=3 threshold shortly afterward and remained elevated for a prolonged period, signifying a sustained disturbance. However, the Dst index only dropped to about -47 nT, remaining within the weak storm range. Like the previous event, this storm featured modest magnetospheric activity, as indicated by the shallow depth and short duration of the Dst depression. In both panels, the onset of geomagnetic activity indicated by the brown vertical dotted line were clearly triggered by a southward turning of the IMF Bz, validating the importance of this parameter in storm initiation.

In panel (a), the storm onset occurred around 11:00 UT on April 24th, 2013, where the IMF Bz reached its peak minimum value, marked by a brown vertical dotted line. This was followed by a rise in the Kp index, crossing the yellow horizontal line at Kp=3, indicating the day was geomagnetically disturbed

. The Kp index stayed above this threshold for several hours, confirming the storm's active phase. The Dst index, reflecting storm intensity, dropped below -25 nT (under a blue horizontal dotted line) but stayed near -50 nT, classifying the event as a weak geomagnetic storm. The Dst depression was mild, showing a shallow recovery and limited

ring current intensification.

Panel (b) shows the October 2014 storm onset around 15:00 UT on October 14th, marked by a brown vertical dotted line and a clear southward excursion of IMF Bz. The Kp index rose above the Kp=3 threshold soon after, staying elevated for a long period, indicating a sustained disturbance. The Dst index dropped to about -47 nT, still within the weak storm range. This storm also showed modest magnetospheric activity, demonstrated by the shallow and brief Dst depression.

4.1.2 Statistical analysis of geomagnetic storms.

The statistics indicate that there was a total of 1,082 geomagnetic storms in the period between 2011 and 2016. Out of this number of storms, 822 were weak, 231 were moderate and 29 were severe following the categories by Matamba and Habarulema (2018). These storm statistics are presented in the Figure 4.4.

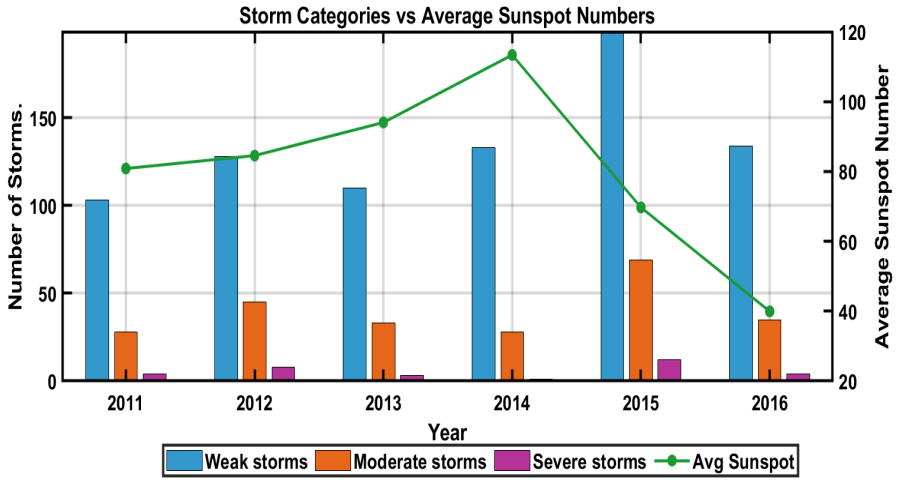

Figure 4.4: Average sunspot number vs storm categories (solar cycle 24)

The Figure 4.4 illustrates the relationship between geomagnetic storm activity and average sunspot numbers over the period of years from 2011 to 2016. The geomagnetic storms were categorised into weak, moderate and severe events and overlayed with the average annual sunspot number. A clear pattern that aligns with solar cycle was observed and both the number of geomagnetic storms and sunspot numbers gradually increased from 2011. The peak was observed around 2014 and then declined towards 2016. Weak storms were the most frequent throughout the period, with a notable peak in 2015 while moderate storms followed a similar trend on a smaller scale. Severe storms were relatively rare and did not show a strong correlation with sunspot numbers. The green line representing average sunspot numbers indicated the solar cycle rising sharply to a peak in 2014 before falling steeply. This alignment reveals a strong relationship between solar activity indicated by sunspot numbers and the occurrence of geomagnetic storms particularly of weak and moderate intensity. Generally, it was observed there was a high chance of occurrence geomagnetic storms during period of high sunspot numbers. This is because sunspots are indicators of intense solar activity. Regions with many sunspots are often associated with solar flares, CMEs and huge bursts of solar wind and magnetic fields (Hathaway, 2015). When these CMEs reach Earth, they disturb the planet's magnetic field and trigger geomagnetic storms. So, more sunspots typically mean a higher likelihood of such solar eruptions and hence increasing the chances of geomagnetic storms (Gopalswamy, 2006).

The geomagnetic storms were further categorised into CIR driven and CME driven storms. The statistics in this study showed that out of 1,082 storms, a total of 1053 storms were CIR driven and only 29 storms were CME driven as indicated in Figure 4.5. It was also observed that out of the 29 CME driven storms only 4 storms were driven by fast Halo CMEs. This is according to CME catalog.

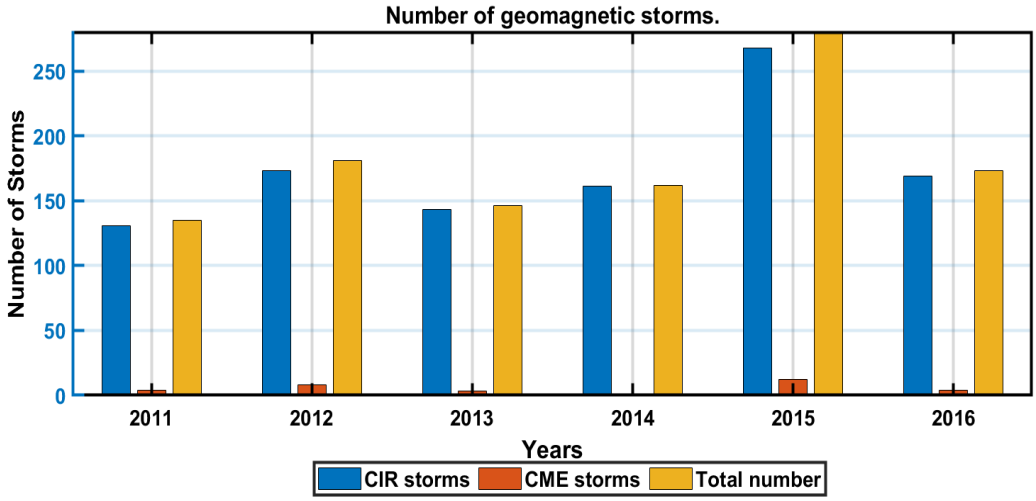

Figure 4.5: Total number of geomagnetic storms (2011-2016)

The annual count of geomagnetic storms from 2011 to 2016, categorized by their origin CIR storms and CME storms, alongside the total number of storms were presented in the bar graph in the Figure 4.5. The bar graph shows that CIR storms (blue bars) overwhelmingly dominate the storm occurrences across all years while CME storms (orange bars) are relatively rare and contribute only a small fraction to the total (yellow bars). The data in this figure is relative to the solar activity trend observed in Figure 4.4. Both figures showed a rise in geomagnetic storm frequency from 2011, peaking around 2015 and then declining towards 2016. The peak in total geomagnetic storms in 2015 aligns with the highest average sunspot numbers from Figure 4.4, this implies that increased solar activity contributed to more frequent geomagnetic disturbances. However, this figure provided a deeper insight into the source of these storms highlighting that CIR-driven storms are the primary contributors, particularly during the declining phase of the solar cycle (post-2015). The rarity of CME storms compared to CIR storms also suggests that while CMEs can cause more intense geomagnetic effects, they are less frequent than CIRs which occur more regularly as part of the solar wind structure. Thus, this figure complements Figure 4.4 by emphasizing that the observed trend in geomagnetic storm frequency is largely driven by CIRs rather than CMEs even during periods of high sunspot activity. Generally, both figures revealed the dominant role of CIRs in driving space weather during the period of study.

4.2 Ionospheric Scintillation Events

This section presents ionospheric scintillation events observed by analysing the SCINDA data obtained from the SCINDA stations Mbarara and Makerere. The results presented in subsection 4.2.1 define a scintillation event. The diurnal variation of amplitude scintillation is presented in subsection 4.2.2 while the annual scintillation statistics in subsection 4.2.3.

4.2.1 The morphology of a scintillation event

The Figures 4.6 and 4.7 present satellite elevation and scintillation data over a 24-hour period. The top panel shows the elevation angles of multiple satellites, each represented by a colored arc. These arcs mostly remain above the 30° elevation threshold. This is essential for ensuring reliable GPS signal reception by reducing the effects of atmospheric interference and multipath effect providing continuous and reliable sky coverage. The bottom panel illustrates the S4 index, a metric used to quantify signal amplitude scintillation caused by ionospheric irregularities.

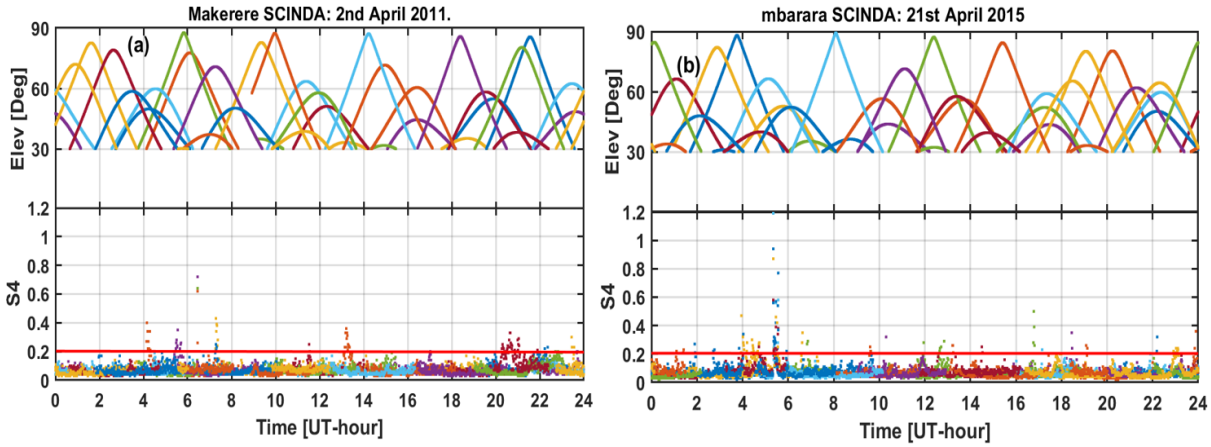

Figure 4.6: Background signal levels for scintillation index (S4)

Figure 4.6 (a) indicates a plot from Makerere SCINDA on 2nd April 2011. It displays that S4 index predominantly remained below 0.2 marked by a red horizontal line, indicating background noise and generally quiet ionospheric conditions. The Instances where S4 values lied above the red horizontal line were short lived and remained within the 0.2 to 0.4 range, classifying them as minor scintillation events. These weak disturbances occurred briefly in the early morning (04:00–07:00 UT), around midday (13:00 UT), and during the early night hours (20:00–22:00 UT). Given their limited duration and low intensity, these minor scintillations had no significant effect on signal quality and are typical of weak low latitude ionospheric irregularities. Figure 4.6 (b) shows a SCINDA plot from Mbarara on 21st April 2015. As with Figure 4.6 (a), satellites tracked by the receiver maintain elevation angles above 30°, ensuring reliable signal coverage throughout the day. The S4 index remained predominantly below 0.2, indicating background noise level and

overall quiet ionospheric conditions. However, brief instances of minor scintillation were seen early in the morning between 04:00–06:00 UT, with isolated S4 values exceeding 0.4 and a few even surpassing 1.0, suggesting short-lived but locally stronger irregularities more pronounced than those seen in the Makerere data. These elevated S4 values, although short in duration, may have been caused by localized and transient equatorial plasma irregularities, possibly triggered by residual post-midnight instabilities or weak early morning electrodynamic processes. The dominant background scintillation (S4 $<$ 0.2) throughout most of the day and night reflects a stable ionospheric environment, which is typically maintained by low geomagnetic activity, the absence of post-sunset equatorial plasma bubbles and steady solar ionization during the daytime. Such calm conditions are also favored during periods of low solar and geomagnetic disturbance and during times when large-scale ionospheric instabilities are not supported by seasonal drivers. In summary, both the Makerere and Mbarara observations reflect predominantly quiet ionospheric conditions with background level scintillation, though Mbarara recorded slightly stronger early morning activity. These similarities highlight the generally stable ionospheric behavior in the lower latitude region under quiet space weather conditions.

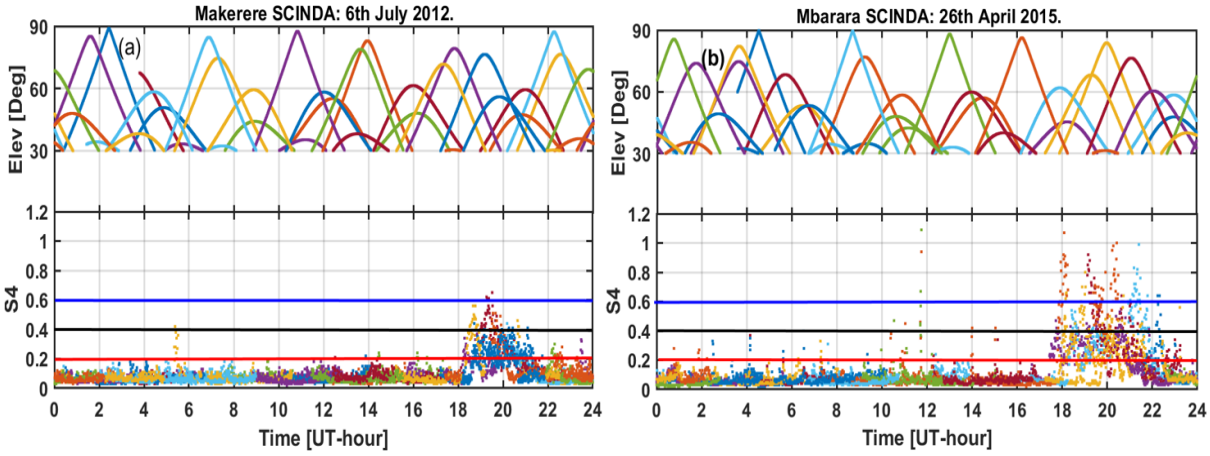

Figure 4.7: Identified significant scintillation events ($S4 > 0.2$)

The figure 4.7 (a) indicates plots from Makerere SCINDA station on 6th July 2012. This figure provides a valuable insight into the diurnal behavior of satellite elevation angles and S4 index in the lower latitude environment. The top panel demonstrates that most GPS satellite tracks maintain elevation angles above 30°, a threshold that helps reduce signal distortion due to atmospheric and multipath effects. In the bottom panel, the S4 was plotted over Universal Time (UT). Reference lines at S4 = 0.2 (red), 0.4 (black), and 0.6 (blue) demarcate scintillation intensity levels. S4 values below the red line indicate background noise with no significant scintillation, those between the red and black lines suggest weak scintillation, values between the black and blue lines represent moderate scintillation, and readings above the blue line reflect strong scintillation events. From 00:00 to 17:00 UT, most S4 values remain below 0.2, indicating quiet ionospheric

conditions. However, between 18:00 and 22:00 UT, there is a marked increase in scintillation activity, with several S4 values crossing into the weak and moderate categories, and a few nearing the strong scintillation threshold. This evening enhancement aligns with the known lower latitude ionospheric behavior, where post-sunset instabilities driven by the PRE of the eastward electric field generate plasma irregularities that disrupt signal amplitude.

The observations from Mbarara SCINDA station on 26th April 2015 indicated in Figure 4.7 (a) complemented the Makerere findings, reinforcing the recurring evening pattern of scintillation in the East African lower latitude region. The elevation angles in the top panel again show that most satellite paths exceeded the 30° threshold, ensuring high-quality signal reception. The S4 index in the bottom panel is similarly plotted with reference lines at 0.2 (red), 0.4 (black), and 0.6 (blue), defining background noise, weak, moderate, and strong scintillation levels respectively. As with Makerere, the early hours from 00:00 to 17:00 UT exhibit minimal scintillation, with S4 values staying within the background noise range. Beginning around 18:00 UT, S4 values noticeably rise, many exceeding the 0.2 threshold and several surpassing 0.6, indicating strong scintillation events. The consistency of this post-sunset scintillation behavior across both stations highlights the influence of PRE driven electric fields that intensify ionospheric instabilities in the equatorial F-region after local sunset. These instabilities give rise to plasma bubbles that disturb GPS signal amplitude. The patterns observed in both stations, especially during periods of elevated solar activity, underscore the dynamic and predictable nature of lower latitude scintillation driven by solar and geomagnetic influences, with clear thresholds distinguishing levels of signal degradation. These moderate and strong events observed are potential to causing severe signal fluctuation and sometimes complete signal blackouts. They lead to significant loss of lock in GNSS systems hence affecting positioning and satellite navigation (Carrano et al., 2012). The weak scintillation events are potential to causing minor amplitude variation and result in signal fading. They typically do not completely lead to signal loss but may reduce accuracy or introduce small errors. The errors caused by weak scintillations are not significant and can be easily fixed by setting a lock threshold on GPS receiver system's bandwidth (Carrano et al., 2012).

4.2.2 Diurnal Variation

The two panels (a) and (b) of the Figure 4.8 illustrate the diurnal variation of S4 index for all satellites observed at elevation angles above 30°, over a month-long period. Panel (a) presents data from SCINDA station MBA for April 2012, while panel (b) represents data from SCINDA station MAK for May 2015. The red horizontal line at S4 = 0.2 indicates the lower threshold distinguishing background noise from significant scintillation. Values below this line are considered non-scintillating (background noise), while those above it

indicate actual scintillation activity.

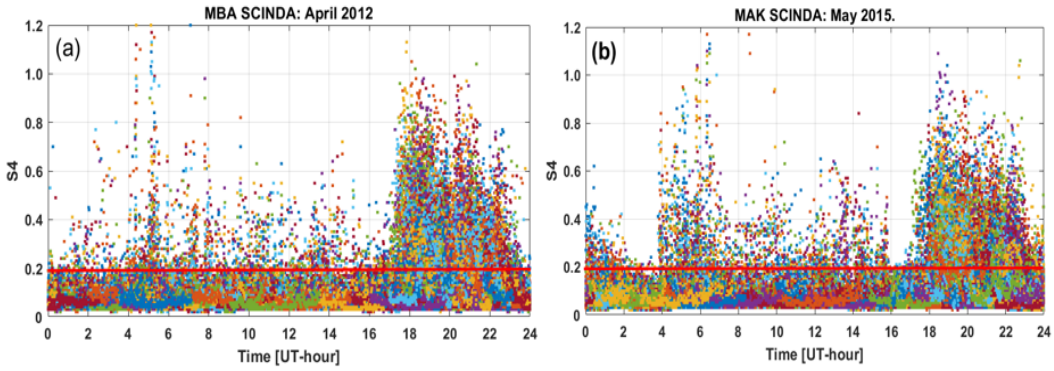

Figure 4.8: Diurnal variation of amplitude scintillation (Mbarara and Makerere)

In Figure 4.8 (a), corresponding to scintillation data from SCINDA station MBA for April 2012, indicates that significant scintillation activity occurs predominantly during the nighttime hours, particularly between 18:00 and 24:00 UT. During these night hours, S4 values frequently exceed the 0.2 threshold, with occasional values nearing or exceeding 1.0, indicating very strong amplitude scintillation. This is a typical pattern in the low-latitude regions, where post-sunset ionospheric irregularities lead to the formation of EPBs (Dungey, 1956). These plasma bubbles result from the Rayleigh–Taylor instability and can they cause amplitude scintillation. A secondary but less pronounced cluster of elevated S4 values appeared between 05:00 and 07:00 UT, which could represent lingering irregularities from the previous night or early morning transitional phenomena. Scattered instances of daytime scintillation are also observed, although they are rare and mostly remain close to the background noise threshold.

Figure 4.8 (b), represents scintillation data from MAK SCINDA station for May 2015. It displays a similar overall pattern with strong scintillation concentrated in the post-sunset period between 18:00 and 24:00 UT. However, compared to MBA, the scintillation activity at MAK appears slightly more prolonged and intense, with more data points exceeding S4 values of 1.0. Notably, Figure 4.8 (b) also shows a broader spread of daytime scintillation events, with several scattered values above 0.2 occurring between 04:00 and 14:00 UT. This implies that the region around Makerere experienced more frequent daytime irregularities during this month. These daytime scintillation events, although less intense than the nighttime occurrences, are of interest due to their unexpected timing under typically stable ionospheric conditions.

The nighttime scintillations observed in both plots are attributed primarily to EPBs, which are driven by post-sunset F-region ionospheric instabilities (Dungey, 1956). These bubbles form and rise through the ionosphere, disrupting the propagation of radio signals and causing significant amplitude fluctuations Amabayo et al. (2014). It should be noted

that the GPS receivers employed in this study were located in an elevated semi-arid region. These areas typically have minimal green vegetation cover. Therefore, setting a signal ray path elevation angle threshold of 30° was sufficient to eliminate all scintillation occurrences resulting from multipath effects and line-of-sight obstructions caused by vegetation and terrain, as highlighted in Amabayo et al. (2014). This verifies that the recorded post-sunset scintillation events in the GPS L-band navigation signals were solely due to ionospheric irregularities which are predominantly active at night (Martiningrum et al., 2022).The variation in duration and intensity of these nighttime events between the two sites are influenced by differences in geographical location, local ionospheric conditions, geomagnetic activity and seasonal factors Perkins (1975). Daytime scintillations appeared in both datasets but were less frequent and weaker. They are not linked to ionospheric irregularities, which mostly occur after sunset and before sunrise. These daytime effects are mainly caused by several factors, especially Atmospheric Gravity Waves (AGWs) (Jimoh et al., 2022). AGWs start in the lower atmosphere and travel upward, disturbing the ionosphere and creating plasma irregularities during the day. They are common in low latitude areas due to high diurnal humidity, particularly during equinox months (Jimoh et al., 2022). The plots confirm that amplitude scintillation is mainly a nighttime event caused by equatorial plasma instabilities. Still, daytime scintillations in the MAK dataset show the influence of secondary processes like atmospheric gravity waves.

4.2.3 Annual and Seasonal Variability

This section shows the yearly frequency of scintillation events and the data availability by the number of days with data each month.
The statistical analysis uses the percentage of scintillation occurrences to demonstrate monthly, annual, and diurnal variation trends.

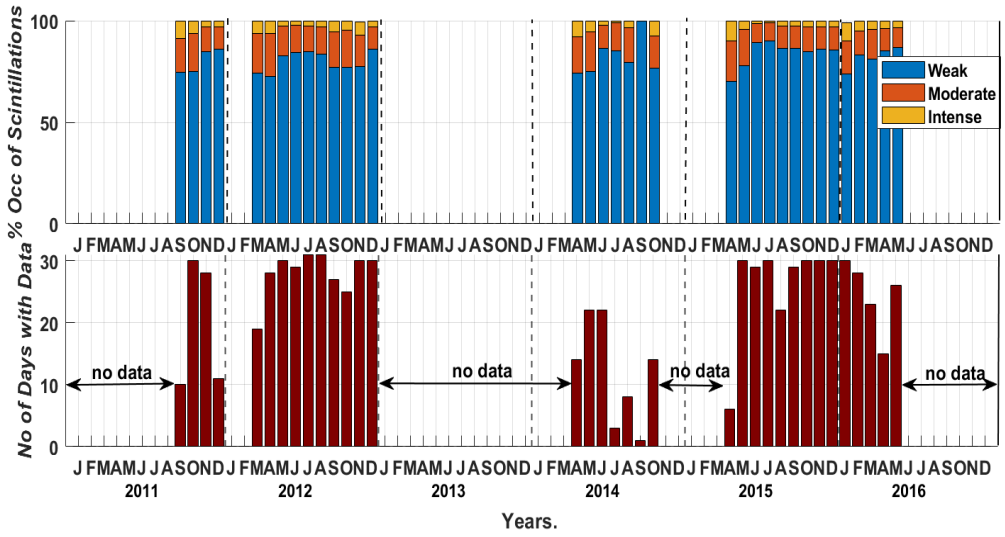

Figure 4.9: Monthly variability of scintillation occurrence (Mbarara station)

Figure 4.9 (a) depicts the monthly percentage of scintillation events and their intensity at Mbarara from 2011 to 2016, along with the number of days with data each month. The top panel indicates that weak scintillations were most common, while moderate and intense events were infrequent. The figure also shows that the occurrence of strong scintillations was generally low, with peaks in April 2014 and April 2015. The peaks of percentage of occurrence of moderate scintillation events were observed in March 2012 and March 2015. Scintillation occurrence generally exceeded 80% in months with data indicating frequent ionospheric activity. However, significant data gaps were evident, including the entire year of 2013 and parts of 2011, 2014, and 2016. The bottom panel highlighted data availability with 2012 and 2015 providing the most complete records. Despite the predominance of weak scintillations, their persistent nature suggested potential implications for satellite communication and GPS reliability.
Moderate and strong scintillations to occurred far less frequently compared to weak scintillations throughout the period from 2011 to 2016. The stacked bar segments representing moderate (orange) and strong (yellow) events were consistently small with avarages of 7% and 0.5% respectively. This implies that these higher-intensity scintillations contribute only a minor fraction to the total scintillation activity for the SCINDA data obtained from Mbarara. When they did appear, moderate scintillations were slightly more common than strong ones but still occurred sporadically. The relative scarcity of strong scintillation

events implied that severe ionospheric disturbances were not at this location. This pattern reflects the regional ionospheric conditions or geomagnetic latitude of Mbarara which may not favor the frequent development of irregularities that cause scintillations. The Figure 4.10 indicated Similar results for the annual probability of occurrence of scintillation events as observed at SCINDA station in Makerere.

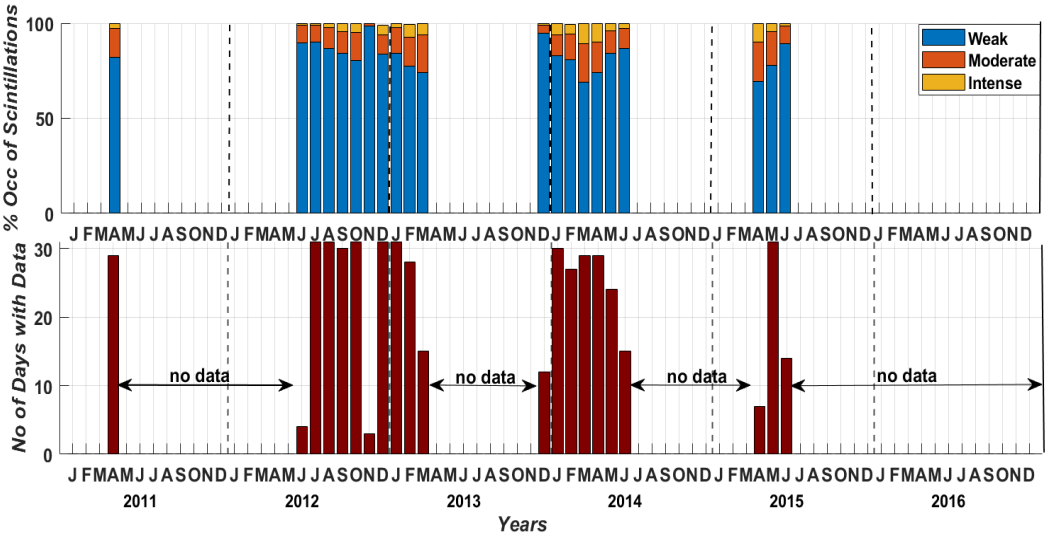

Figure 4.10: Monthly variability of scintillation occurrence (Makerere station)

Figure 4.10 (b) presented the monthly percentage of occurrence of scintillation for the data obtained from Makerere for a period from 2011 to 2016 along with the number of days data was available each month. The data revealed that weak scintillations (depicted in blue) overwhelmingly dominated across all observed periods with an average of 85% while moderate (orange) and strong (yellow) scintillations are rare. Moderate scintillations occasionally appear alongside periods of high weak scintillation activity particularly in March and April 2012, September 2013, and April 2015. This implied that the occurrence of scintillation events is highly associated with specific seasonal or geomagnetic conditions. Strong scintillation events were nearly absent indicating that strong ionospheric disturbances were not frequent. The presence of moderate scintillations of an average of 9% implied that the ionospheric environment over Makerere was generally unstable during the study period. This has got a negative implication for GNSS reliability in the region but also highlights the need for continuous monitoring to better understand and capture less frequent, higher impact scintillation events (Abadi et al., 2014).

4.3 Scintillation events during geomagnetic storms

The results of this study indicate three storm cases that were observed by matching the scintillation events with geomagnetic storm. These storm cases present the rightful geomagnetic storm conditions that influence the occurrence of scintillation events as

discussed in subsection 4.3.1.

4.3.1 Case Studies of Storms

Case study 1.

Storm case 1 presents geomagnetic storm conditions that triggered ionospheric irregularities which caused strong scintillation events as illustrated in Figure 4.13.

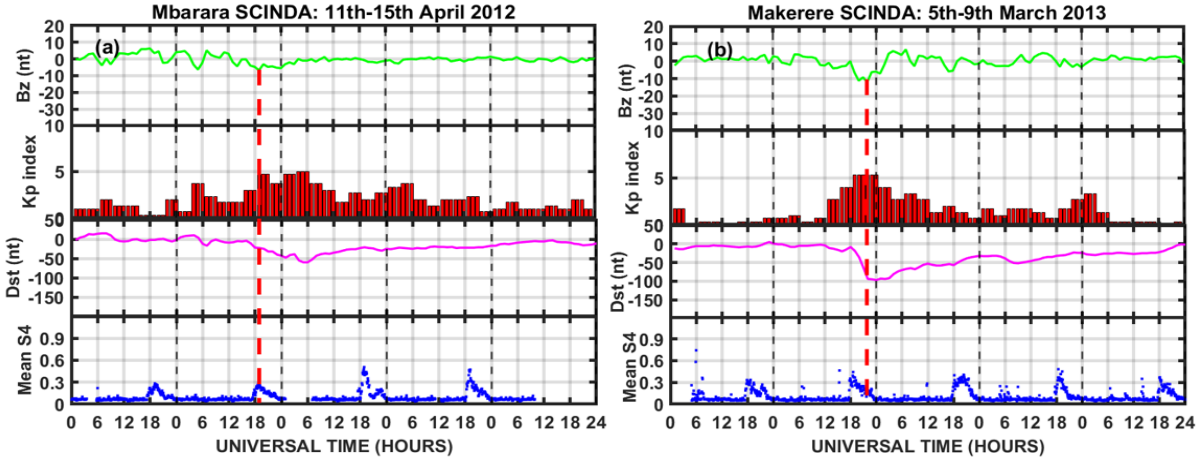

Figure 4.11: Case Study 1: Storm-scintillation relationship for 11th-15th April 2012 and 5th-9th March 2013 geomagnetic storms

Figure 4.13(a) depicts a geomagnetic storm from April 11th to 15th, 2012. The top panel shows the IMF Bz component turning southward around 12:00 UT on April 12th, reaching a minimum of -8 nT at 19:00 UT the same day. This time, marked by a red vertical dotted line, indicates the storm onset. The IMF Bz stayed mostly southward for several hours before shifting northward around 10:00 UT on April 13th. Below, the Kp index remained above 3 on April 11th and 12th, indicating geomagnetically disturbed days. The Dst index varied between -25 nT and -72 nT, classifying the event as a moderate geomagnetic storm. The bottom panel shows average S4 for all visible PRNs at Mbarara GPS station on April 13th, 2012. Strong scintillations ($S4 > 0.3$) occurred on the nights of April 13th and 14th, aligning with the storm's recovery phase.

Figure 4.13(b) presents another geomagnetic storm that occurred between 5th and 9th March 2013. The IMF Bz component gradually turned southward before it attained its minimum peak value of -12 nT at around 22:00 UT on 6th March 2013. This was the time of commencement of the geomagnetic storm as indicated by a red dotted vertical line. It then briefly returned northward before turning southward again on 7th March and then northward for the rest of the storm days . The Kp index reached a peak value of 3 on 6th March, signifying a storm-disturbed day. Dst index recorded a minimum of -100 nT at around 00:00 UT on 6th March, indicating a severe geomagnetic storm. The bottom panel shows the average GPS S4 recorded at the Makerere for all visible satellites

during this storm period. Strong scintillation events with average S4>0.3 were observed during the nights of 6th, 7th and 8th March 2013, aligning with the recovery phase of the storm.

Case study 2.

Storm case 2 is presented in the Figure 4.12 (a) and (b) indicates moderate scintillation events for scintillation data over Mbarara and Makerere SCINDA stations.

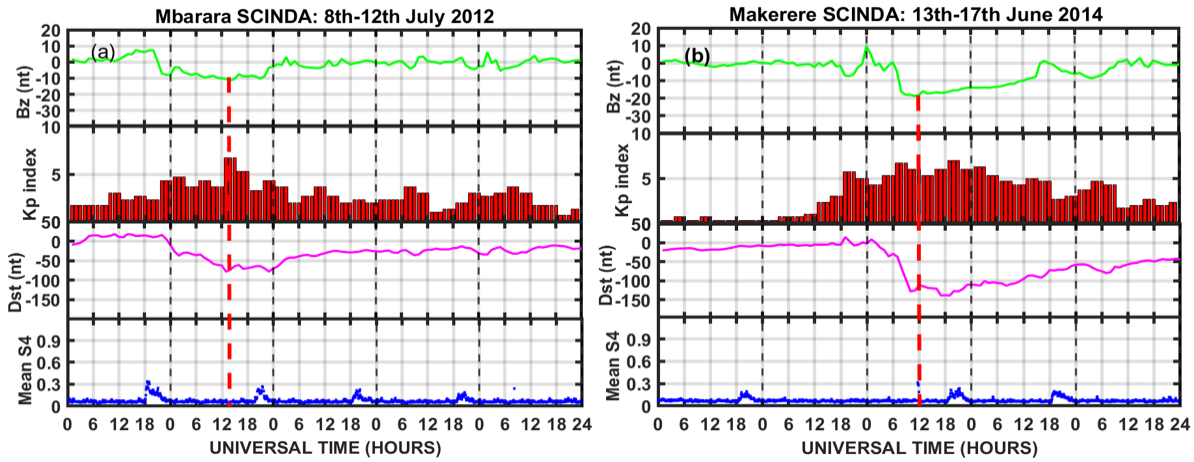

Figure 4.12: Case Study 2: Storm-scintillation relationship for 8th-12th July 2012 and 13th-17th June 2014 geomagnetic storms

Figure 4.12(a) shows the effects of a moderate geomagnetic storm from July 8th to 12th, 2012. On July 9th, the IMF Bz component had a prolonged southward excursion, reaching about -11 nT near 13:00 UT. This peak southward turning, marked by a red vertical dotted line, indicates the storm onset (bow shock time). The Kp index sharply rose to 8 that day, signaling a disturbed geomagnetic state. The second-bottom panel shows the Dst index dropping to -80 nT, confirming the event as a moderate geomagnetic storm. The bottom panel depicts mean amplitude scintillation at the SCINDA station in Mbarara for all visible satellites during the storm. Weak scintillations, with average values between $0.14 \leq 0.3$, occurred on the nights of July 9th to 12th, gradually weakening over consecutive nights.

Figure 4.12(b) shows another storm-disturbed period spanning 13th to 17th June 2014. The IMF Bz turned southward on 15th June and marked the time of commencement of the storm at 12:00 UT as indicated by a red vertical dotted line at its minimum peak value. The Kp index again rose past a value of 3 on 14th June. It remained above this threshold until 17th June indicating enhanced geomagnetic storm days. The Dst index reached a minimum value of -149 nT during this period, categorizing the event as a severe geomagnetic storm. The bottom panel displays the average amplitude scintillation recorded at the SCINDA station in Makerere. Weak scintillation activity was observed

on the night of 15th June while diminishing towards the night of 16th to eventually show no scintillation on 17th. These events took place during the recovery phase of the storm.

Case study 3.

Figure 4.13 presents case study 3 condition of no or very weak scintillation occurrence during geomagnetic storm period.

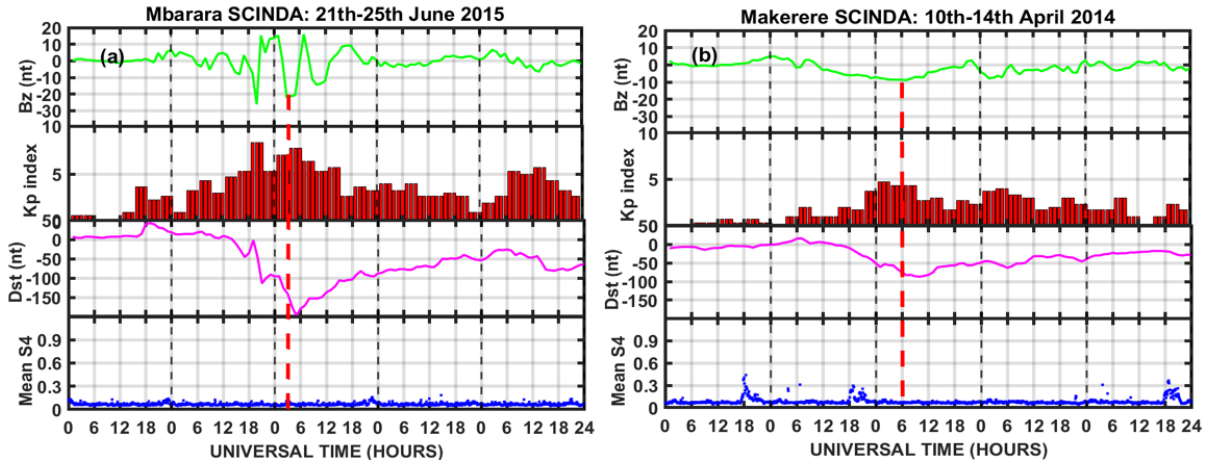

Figure 4.13: Case Study 3: Storm-scintillation relationship for 21st-25th June 2015 and 10th-14th April 2014 geomagnetic storms

Figure 4.13(a) illustrates the effects of a severe geomagnetic storm that occurred between 21st and 25th June 2015. The top panel shows that the IMF Bz component fluctuated between northward and southward directions before undergoing a prolonged southward excursion, reaching a minimum value of -22 nT at 03:00 UT on 23rd June indicating the time of commencement of the storm. This southward orientation persisted for several hours before turning northward at approximately 03:25 UT, marked by a red vertical dotted line. Correspondingly, the Kp index rose to a maximum value of 8, indicating a storm disturbed day. The second-last panel displays the Dst index, which recorded a significant negative peak of -200 nT at 05:00 UT, confirming the severity of the storm. Despite the intense geomagnetic conditions and extended recovery phase, no GPS amplitude scintillation events were observed during the storm period, as shown in the bottom panel, which presents average S4 from 21st to 25th June 2015.

Figure 4.13(b) presents the effects of a moderate geomagnetic storm that took place between 10th and 14th April 2014. This storm was initiated by a southward turning of the IMF Bz, which reached a minimum of -9 nT at 06:00 UT on 11th April. This epoch marked the time of commencement of the the storm as indicated in the top panel by a red vertical dotted line. A Kp curve above 3 was recorded on the same day, signifying a storm-disturbed condition. The second-last panel shows that the Dst index dropped to a minimum of -98 nT on 12th April, consistent with a moderate storm classification.

The bottom panel illustrates the amplitude scintillation activity recorded over the same period. Scintillation events were observed during the nights of 10th and 11th April, while no scintillation was recorded on the following two storm days. However, very weak scintillations reappeared during the third day of the recovery phase.

A broader analysis of geomagnetic storms and their associated effects was conducted by categorizing storm events into three case types (Cases 1, 2, and 3) based on their severity and impact. The study identified 18 geomagnetic storms that occurred between 2011 and 2016, a period during which SCINDA data were consistently available from the Mbarara and Makerere ground stations. These events were systematically summarized in Table 4.1, providing detailed insights into the corresponding geomagnetic indices and GPS scintillation responses.

Table 4.1: Summary of geomagnetic storms events and corresponding scintillation observations

No	0nset date	Bow-shock time (UT)	Min Dst (nT)	Station	Scintillation status
1	24th Oct 2011	00:00	-180	MBA	Strong scintillation
2	12th Apr 2012	19:00	-60	MBA	Strong scintillation
3	12th Mar 2012	20:00	-75	MBA	Strong scintillation
4	6th Mar 2013	22:00	-80	MAK	Strong scintillation
5	23rd Apr 2016	19:00	-125	MBA	Strong scintillation
6	13th May 2015	18:00	-80	MBA	Strong scintillation
7	27th Mar 2012	23:00	-70	MBA	Strong scintillation
8	6th Aug 2012	15:00	-55	MAK	Strong scintillation
9	6th Apr 2011	14:00	-60	MAK	Weak scintillation
10	9th Jul 2012	13:00	-72	MBA	Weak scintillation
11	15th Jun 2014	13:00	-78	MAK	Weak scintillation
12	3rd Jul 2012	13:00	-80	MAK	Weak scintillation
13	12th Jun 2014	14:00	-70	MBA	Weak scintillation
14	15th Jul 2012	12:00	-145	MAK	Weak scintillation
15	12th Apr 2014	06:00	-90	MAK	No scintillation
16	22nd Jun 2015	03:00	-80	MBA	No scintillation
17	13th Jun 2015	03:00	-200	MBA	No scintillation
18	11th May 2015	07:00	-65	MAK	No scintillation

The Table 4.1 presents a dataset of 18 geomagnetic storm events, detailing each event's onset date, bow shock time (UT), minimum Dst index (nT), station of observation and the associated scintillation status. The Dst index, shows that most storms indicated in this table fall within the moderate to severe range, with Dst values ranging between -55 and -200 nT. Over eight strong scintillation events were observed. Their corresponding bow shock time fell between 15:00 UT and 00:00 UT thus categorised under storm case 1. Over seven scintillation events were weak. These events were categorised under storm case 2 since their corresponding bow shock time fell between 12:00 UT and 15:00 UT. For the period of when the bow shock time fell between 00:00 UT and 12:00 UT no scintillation event was observed as indicated in the table. This was classified under storm case 3. These storm cases observed provide a compelling insight into how the bow shock time plays a decisive role in the presence or absence of ionospheric scintillation regardless of the intensity of the geomagnetic storms.

The timing of geomagnetic storm onset, specifically the bow shock arrival, plays a critical role in modulating ionospheric responses and subsequent scintillation activity over the East African low-latitude region. During the early morning to daytime period (00:00–12:00 UT, corresponding to 03:00–15:00 LT), the ionosphere experiences elevated background ionization due to intense solar EUV radiation. This high ionospheric conductivity effectively dissipates PPEFs introduced by geomagnetic disturbances, thereby weakening the vertical ExB drifts (Fejer et al., 2008a). As a result, the PRE, a key driver of plasma bubble formation, becomes significantly diminished. The insufficient uplift of the F-layer suppresses the growth of the RTI, preventing the development of plasma density irregularities and leading to minimal or no scintillation activity, as observed in storm case 3. In contrast, the 12:00–15:00 UT window (15:00–18:00 LT) represents a transitional phase from afternoon to pre-sunset, where solar ionization begins to fade. When the bow shock occurs during this interval, PPEFs can still enhance eastward electric fields, although moderately, lifting the F-layer and initiating weak RTI. This results in the formation of small-scale irregularities and weak plasma bubbles that produce moderate scintillation events (Kelley, 2009b). The most pronounced effects, however, occur during the post-sunset to late night period (15:00–00:00 UT, or 18:00–03:00 LT), when ionospheric conductivity rapidly declines due to recombination. A bow shock striking within this window allows PPEFs to penetrate efficiently, leading to a strong PRE and abrupt F-layer uplift. The steep resulting density gradients greatly enhance RTI, promoting the growth of large-scale plasma bubbles that scatter GNSS signals and trigger intense scintillation events (Tsurutani et al., 2004). These observations highlight that the orientation and duration of the interplanetary magnetic field's southward Bz component, particularly when coupled with favorable local time conditions, serve as dominant drivers of ionospheric irregularities (Fejer et al., 1999). While other storm

parameters are relevant, sustained southward IMF Bz remains the most critical factor in determining whether scintillation-inducing irregularities form. Therefore, real-time monitoring of IMF Bz and storm onset timing could significantly enhance the forecasting of ionospheric scintillation, especially over the lower latitude regions like East Africa where these effects are most pronounced.

Chapter 5

Conclusions and Recommendations

This chapter gives a brief summary of the major findings presented in this thesis, the recommendations to help in improving the findings and the future works.

5.1 Conclusions

In this study, scintillation data and Geomagnetic storm data were used to investigate the impact of geomagnetic storm onset time on GNSS reliability. The geomagnetic storms were classified and matched with the corresponding scintillation events.

The statistics indicated that there was a total of 1,082 geomagnetic storms storms in the period between 2011 and 2016. Out of this number of storms, 822 were weak, 231 were moderate and 29 were severe. A deeper insight into the source of these storms highlighted that CIR-driven storms were more frequent than the CME driven storms. A number of geomagnetic storms and their effects were investigated and grouped according to their precise time of commencement (bow shock time).

The analysis of SCINDA data from the Mbarara and Makerere stations revealed that ionospheric scintillation events predominantly occur during quiet ionospheric conditions with background noise levels ($S4 < 0.2$), though Mbarara exhibited slightly stronger early morning scintillation activity. The diurnal variation demonstrated significant post-sunset scintillation enhancement, linked to equatorial plasma instabilities such as equatorial plasma bubbles driven by pre-reversal enhancement (PRE) electric fields. Annual statistics showed that weak scintillations dominated, accounting for over 80% of occurrences, while moderate and strong scintillations were infrequent. These patterns reflect generally stable but dynamically evolving ionospheric behavior in East Africa's low-latitude region, with implications for GNSS reliability, especially during periods of heightened solar and geomagnetic activity. Consistent monitoring is essential to understand these variations and their impact on satellite-based navigation and communication systems.

The investigation revealed that about only 18 geomagnetic storms occurred in the period when SCINDA data were readily available at the stations in Mbarara and Makerere for the period of study. The occurrence of ionospheric scintillation during geomagnetic storm events was more strongly linked and influenced by the time of occurrence of the bow shock (UT) instead of its intensity as measured by the Dst index. Strong scintillation events consistently occurred when the bow shock fell between 15:00 UT and 00:00 UT a period

corresponding to evening hours and post midnight in the low-latitude regions. Weak scintillation events were observed when the time of commencement (bow shock time) laid in a narrower time window between 12:00 UT and 15:00 UT. This time corresponded to the late afternoon and pre-sunset of the lower latitude region. In contrast, no scintillation event was recorded when bow shock occurred between 00:00 UT and 12:00 UT, even during intense geomagnetic storms. These patterns indicated that diurnal variations in ionospheric conditions play a dominant role in scintillation behavior. The occurrence of geomagnetic storms is a secondary factor that modulates and influence the ionospheric irregularities which solely cause scintillation events.

5.2 Limitations of the Study

This study is limited by data gaps in the available scintillation measurements, which may affect the continuity and completeness of the analysis. Additionally, daytime scintillation events were not accounted for, although their impact is generally minor compared to nighttime occurrences. These limitations should be considered when interpreting the results, and efforts to include more continuous and comprehensive datasets in future work are recommended.

5.2.1 Research Recommendations

Future work should focus on developing early warning systems and predictive models that link geomagnetic storm onset timing with scintillation events to anticipate GPS signal degradation and improve navigation resilience. Integrating real-time monitoring of key solar wind parameters like IMF Bz into GNSS services would enhance forecast accuracy. Expanding the study to include regional multi-station observations beyond Mbarara and Makerere will validate findings across the equatorial belt. Employing machine learning and statistical approaches to combine storm indices with bow shock epoch timing is recommended for improved forecasting capabilities. This study should be extended to cover Solar Cycle 25 to capture current and upcoming space weather dynamics. Including phase scintillation ($\sigma\phi$) alongside amplitude scintillation (S4) measurements will provide a more comprehensive understanding of ionospheric disturbances.

References

Aarons, J. (1982). Global morphology of ionospheric scintillations. *Proceedings of the IEEE*, 70(4):360–378.

Aarons, J. (1997). Global positioning system phase fluctuations at auroral latitudes. *Journal of Geophysical Research: Space Physics*, 102(A8):17219–17231.

Abadi, P., Saito, S., and Srigutomo, W. (2014). Low-latitude scintillation occurrences around the equatorial anomaly crest over indonesia. In *Annales Geophysicae*, volume 32, pages 7–17. Copernicus Publications Göttingen, Germany.

Abdu, M. (2005). Equatorial ionosphere–thermosphere system: Electrodynamics and irregularities. *Advances in Space Research*, 35(5):771–787.

Abiriga, F., Amabayo, E. B., Jurua, E., and Cilliers, P. J. (2021). Investigation of the impact of ionospheric scintillation on gnss performance over east africa. *Advances in Space Research*, 68(7):2876–2889.

Adams, A. (2007). Spherical rare-earth magnets in introductory physics. *The Physics Teacher*, 45(7):409–415.

Akala, A. O., Doherty, P. H., Carrano, C. S., Groves, K. M., and Seemala, G. K. (2015). Climatology of gps amplitude scintillations over equatorial africa during the minimum and ascending phases of solar cycle 24. *Astrophysics and Space Science*, 357(1):17.

Ali, A., Tong, J., Ali, H., Mughal, M. R., and Reyneri, L. M. (2020). A detailed thermal and effective induced residual spin rate analysis for leo small satellites. *IEEE Access*, 8:146196–146207.

Amabayo, E. B., Edward, J., Cilliers, P. J., and Habarulema, J. B. (2014). Climatology of ionospheric scintillations and tec trend over the ugandan region. *Advances in Space Research*, 53(5):734–743.

Anderson, D. (1999). *The ionosphere*. Space Environment Center.

Aschwanden, M. J. (2005). *Physics of the Solar Corona: An Introduction*. Springer.

Axford, W. (1962). The interaction between the solar wind and the earth's magnetosphere. *Journal of Geophysical Research*, 67(10):3791–3796.

Bahcall, J. N., Pinsonneault, M., and Basu, S. (2001). Solar models: Current epoch and time dependences, neutrinos, and helioseismological properties. *The Astrophysical Journal*, 555(2):990.

Balogh, A., Beek, T. J., Forsyth, R., Hedgecock, P., Marquedant, R., Smith, E., Southwood, D., and Tsurutani, B. (1992). The magnetic field investigation on the ulysses mission-instrumentation and preliminary scientific results. *Astronomy and Astrophysics Supplement Series (ISSN 0365-0138), vol. 92, no. 2, Jan. 1992, p. 221-236. Research supported by SERC.*, 92:221–236.

Bartels, J., Heck, N. H., and Johnston, H. F. (1939). The three-hour-range index measuring geomagnetic activity. *Terrestrial Magnetism and Atmospheric Electricity*, 44(4):411–454.

Basu, S., Basu, S., Groves, K. M., Yeh, H.-C., Sultan, P. J., and Rich, F. J. (2002a). Gps measurements of ionospheric scintillations in the equatorial region: Relationship to equatorial spread f. *Radio Science*, 37(1):1010.

Basu, S., Basu, S., Groves, K. M., Yeh, H.-F., and Rich, F. J. (1998). Scintillations, plasma drifts, and neutral winds in the equatorial ionosphere after sunset. *Journal of Geophysical Research: Space Physics*, 103(A9):17415–17428.

Basu, S., Groves, K., Basu, S., and Sultan, P. (2002b). Specification and forecasting of scintillations in communication/navigation links: Current status and future plans. *Journal of atmospheric and solar-terrestrial physics*, 64(16):1745–1754.

Biondi, M. A. (1969). Atmospheric electron–ion and ion–ion recombination processes. *Canadian Journal of Chemistry*, 47(10):1711–1719.

Bittencourt, J. and Abdu, M. (1981). A theoretical comparison between apparent and real vertical ionization drift velocities in the equatorial f region. *Journal of Geophysical Research: Space Physics*, 86(A4):2451–2454.

Borduas, N. and Donahue, N. M. (2018). The natural atmosphere. In *Green Chemistry*, pages 131–150. Elsevier.

Borovsky, J. E. and Denton, M. H. (2006). Differences between cme-driven storms and cir-driven storms. *Journal of Geophysical Research: Space Physics*, 111(A7).

Braasch, M. S. (1996). Multipath effects. *Global Positioning System: Theory and Applications*, 1(26):547–568.

Bray, R. J. and Loughhead, R. E. (1964). *Sunspots*. Chapman and Hall. Classic reference on sunspots and solar activity.

Budden, K. (1985). *The Propagation of Radio Waves: The Theory of Radio Waves of Low Power in the Ionosphere and Magnetosphere*. Cambridge University Press.

Burch, J. (1974). Observations of interactions between interplanetary and geomagnetic fields. *Reviews of Geophysics*, 12(3):363–378.

Burch, J. L., Winningham, J. D., and Frahm, R. A. (2014). The near-earth plasma environment. Technical report, NASA.

Carrano, C. S., Groves, K. M., and Caton, R. G. (2012). The effect of phase scintillations on the accuracy of phase screen simulation using deterministic screens derived from gps and altair measurements. *Radio Science*, 47(04):1–16.

Carrington, R. C. (1863). *Observations of the spots on the Sun: from November 9, 1853, to March 24, 1861, made at Redhill*. Williams and Norgate.

Center, N. C. D. (2023). Soho/lasco cme catalog. `https://cdaw.gsfc.nasa.gov/CME_list/`. Accessed: 2025-07-05.

Chernosky, E. J. and Hagan, M. (1958). The zurich sunspot number and its variations for 1700–1957. *Journal of Geophysical Research*, 63(4):775–788.

Conker, R. S., El-Arini, M. B., Hegarty, C. J., and Hsiao, T. (2000). Modeling the effects of ionospheric scintillation on gps/sbas availability. In *Proceedings of the IAIN World Congress and the 56th Annual Meeting of The Institute of Navigation (2000)*, pages 563–576.

Cranmer, S. R. (2009). Coronal holes. *Living reviews in solar physics*, 6(1):3.

Daglis, I. A. (2006). Ring current dynamics. *Space science reviews*, 124:183–202.

Daglis, I. A., Thorne, R. M., Baumjohann, W., and Turner, N. (1999). The terrestrial ring current: Origin, formation, and decay. *Reviews of Geophysics*, 37(4):407–438.

Datta-Barua, S., Doherty, P., Delay, S., Dehel, T., and Klobuchar, J. A. (2003). Ionospheric scintillation effects on single and dual frequency gps positioning. In *Proceedings of the 16th international technical meeting of the satellite division of the institute of navigation (ION GPS/GNSS 2003)*, pages 336–346.

Davies, K. (1990). *Ionospheric Radio*, volume 31 of *IEE Electromagnetic Waves Series*. IET (Institution of Engineering and Technology).

Demyanov, V. V., Sergeeva, M. A., and Yasyukevich, A. S. (2019). Gnss high-rate data and the efficiency of ionospheric scintillation indices. *Satellites missions and technologies for geosciences*, pages 1–19.

Du, J., Caruana, J., Wilkinson, P., Thomas, R., and Cervera, M. (2000). Determination of equatorial ionospheric scintillation s4 by dual frequency gps. In *Workshop, La Trobe University, Australia, URSI Commission G*.

Dubey, S., Wahi, R., Mingkhwan, E., and Gwal, A. (2005). Study of amplitude and phase scintillation at gps frequency. *94.20. S; 94.20. J.*

Dugassa, T., Habarulema, J. B., and Nigussie, M. (2019). Longitudinal variability of occurrence of ionospheric irregularities over the american, african and indian regions during geomagnetic storms. *Advances in Space Research*, 63(8):2609–2622.

Dumbović, M. (2015). *Analysis and forecasting of coronal mass ejection space weather effects*. PhD thesis, Prirodoslovno-matematički fakultet, Zagreb.

Dungey, J. (1956). The influence of the geomagnetic field on turbulence in the ionosphere. *Journal of Atmospheric and Terrestrial Physics*, 8(1-2):39–42.

Dungey, J. W. (1961). Interplanetary magnetic field and the auroral zones. *Physical Review Letters*, 6(2):47.

Eastwood, J., Hietala, H., Toth, G., Phan, T., and Fujimoto, M. (2015). What controls the structure and dynamics of earth's magnetosphere? *Space Science Reviews*, 188:251–286.

Engebretson, M. J., Jorgensen, J. L., and Newell, P. T. (2003). Geomagnetic storms. *Space Science Reviews*, 109(1-4):237–277.

Fairfield, D. H. (1971). Average and unusual locations of the earth's magnetopause and bow shock. *Journal of Geophysical Research*, 76(28):6700–6716.

Fejer, B. G., Jensen, J. W., and Su, S.-Y. (2008a). Quiet time equatorial f region vertical plasma drift model derived from rocsat-1 observations. *Journal of Geophysical Research: Space Physics*, 113(A5).

Fejer, B. G., Jensen, J. W., and Su, S.-Y. (2008b). Seasonal and longitudinal dependence of equatorial disturbance vertical plasma drifts. *Geophysical Research Letters*, 35(20).

Fejer, B. G., Scherliess, L., and De Paula, E. (1999). Effects of the vertical plasma drift velocity on the generation and evolution of equatorial spread f. *Journal of Geophysical Research: Space Physics*, 104(A9):19859–19869.

Frey, H. U., Mende, S. B., Immel, T. J., Gerard, J.-C., Hubert, B., Spann, J. F., Gladstone, G. R., Fuselier, S. A., and Burch, J. L. (2003). Continuous magnetic reconnection at earth's magnetopause. *Nature*, 426(6966):533–537.

Ganushkina, N. Y., Liemohn, M., and Dubyagin, S. (2018). Current systems in the earth's magnetosphere. *Reviews of Geophysics*, 56(2):309–332.

Glatzmaier, G. A. and Roberts, P. H. (1995). A three-dimensional convective dynamo solution with rotating and finitely conducting inner core and mantle. *Physics of the Earth and Planetary Interiors*, 91(1-3):63–75.

Gonzalez, W., Joselyn, J.-A., Kamide, Y., Kroehl, H. W., Rostoker, G., Tsurutani, B. T., and Vasyliunas, V. (1994). What is a geomagnetic storm? *Journal of Geophysical Research: Space Physics*, 99(A4):5771–5792.

Goodman, J. M. (2005). *Space Weather and Telecommunications*. Springer Science and Business Media.

Gopalswamy, N. (2006). Coronal mass ejections and space weather. In *Space Weather*, pages 201–251. Springer.

Gopalswamy, N. (2017). Extreme solar eruptions and their space weather consequences. *arXiv preprint arXiv:1709.03165*.

Gopalswamy, N., Yashiro, S., Michalek, G., Stenborg, G., Vourlidas, A., Freeland, S., and Howard, R. (2009). Halo coronal mass ejections and geomagnetic storms. *Earth, Moon, and Planets*, 104(1-4):295–313.

Gradwell, D. P. (2006). The earth's atmosphere. *Ernsting's Aviation Medicine, 4E*, page 1.

Groves, K., Basu, S., and Basu, S. (1997). Ionospheric scintillation and its effect on gps. *Proceedings of the IEEE*, 85(2):211–218.

Gubbins, D. (2008). The geodynamo and magnetic field of the earth. *Reports on Progress in Physics*, 71(4):046301.

Gulyaeva, T. (2003). International standard model of the earth's inosphere and plasmasphere. *Astronomical & Astrophysical Transactions*, 22(4-5):639–643.

Guo, K., Aquino, M., and Vadakke Veettil, S. (2019). Ionospheric scintillation intensity fading characteristics and gps receiver tracking performance at low latitudes. *GPS Solutions*, 23(2):43.

Harrison, R., Hildner, E., Hundhausen, A., Sime, D., and Simnett, G. (1990). The launch of solar coronal mass ejections: Results from the coronal mass ejection onset program. *Journal of Geophysical Research: Space Physics*, 95(A2):917–937.

Hathaway, D. H. (2015). The solar cycle. *Living Reviews in Solar Physics*, 12(1):1–87.

He, J. H., Mendillo, M. J., and Immel, T. J. (2003). Neutral hydrogen density profiles derived from geocoronal imaging. *Journal of Geophysical Research: Space Physics*, 108(A11).

Hlubek, N., Berdermann, J., Wilken, V., Gewies, S., Jakowski, N., Wassaie, M., and Damtie, B. (2014). Scintillations of the gps, glonass, and galileo signals at equatorial latitude. *Journal of Space Weather and Space Climate*, 4:A22.

Hofmann-Wellenhof, B., Lichtenegger, H., and Wasle, E. (2007). *GNSS – Global Navigation Satellite Systems: GPS, GLONASS, Galileo, and more*. Springer Science & Business Media.

Huang, C.-S., Wilson, G. R., Hairston, M. R., Zhang, Y., Wang, W., and Liu, J. (2016a). Equatorial ionospheric plasma drifts and o+ concentration enhancements associated with disturbance dynamo during the 2015 st. patrick's day magnetic storm. *Journal of Geophysical Research: Space Physics*, 121(8):7961–7973.

Huang, C. Y.-Y., Huang, Y., Su, Y.-J., Sutton, E. K., Hairston, M. R., and Coley, W. R. (2016b). Ionosphere-thermosphere (it) response to solar wind forcing during magnetic storms. *Journal of Space Weather and Space Climate*, 6:A4.

Hundhausen, A. (1999). Coronal mass ejections. In *The many faces of the Sun: A summary of the results from NASA's Solar maximum mission*, pages 143–200. Springer.

Jiao, Y. and Morton, Y. T. (2015). Comparison of the effect of high-latitude and equatorial ionospheric scintillation on gps signals during the maximum of solar cycle 24. *Radio Science*, 50(9):886–903.

Jimoh, E. A., Oladipo, O. A., Oyeyemi, E. O., Adewale, A. O., and Olayanju, G. M. (2022). Irregularities in the african ionosphere associated with total electron content anomalies observed during high solar activity levels. *Frontiers in Astronomy and Space Sciences*, 9:947473.

Jurua, E., Andima, G., Oleni, P., and Amabayo, E. B. (2024). Analysis of the scintillation characteristics on the different satellite links derived from gps observations and scinda data over mbarara. *Journal of Atmospheric and Solar-Terrestrial Physics*, 265:106353.

Kappenman, J. G. (2005). An overview of the impulsive geomagnetic field disturbances and power grid impacts associated with the violent sun-earth connection events of 29–31 october 2003 and a comparative evaluation with other contemporary storms. *Space Weather*, 3(8).

Kelley, M. C. (2009a). Earth's ionosphere: Plasma physics and electrodynamics. *International Geophysics Series*, 96.

Kelley, M. C. (2009b). *The Earth's ionosphere: Plasma physics and electrodynamics*. Academic press.

Kelly, J., Dalla, S., and Laitinen, T. (2012). Cross-field transport of solar energetic particles in a large-scale fluctuating magnetic field. *The Astrophysical Journal*, 750(1):47.

Kikuchi, T., Hashimoto, K. K., and Nozaki, K. (2008). Penetration of magnetospheric electric fields to the equator during a geomagnetic storm. *Journal of Geophysical Research: Space Physics*, 113(A6).

Kintner, P. M., Coster, A., Fuller-Rowell, T., and Mannucci, A. J. (2007a). Overview of Mid-latitude Ionospheric Storms. *EOS Transactions AGU*, 88(37):358–359.

Kintner, P. M. and Ledvina, B. M. (2005). The ionosphere, radio navigation, and global navigation satellite systems. *Advances in Space Research*, 35(5):788–811.

Kintner, P. M., Ledvina, B. M., and De Paula, E. (2007b). Gps and ionospheric scintillations. *Space weather*, 5(9).

Kivelson, M. G. and Russell, C. T. (1995). *Introduction to space physics*. Cambridge university press.

Kozyra, J. U. and Liemohn, M. W. (2003). Ring current energy input and decay. *Magnetospheric Imaging—the Image Prime Mission*, pages 105–131.

Kull, H.-J. (1991). Theory of the rayleigh-taylor instability. *Physics reports*, 206(5):197–325.

Laštovička, J., Akmaev, R., Beig, G., Bremer, J., and Emmert, J. (2006). Global change in the upper atmosphere. *Science*, 314(5803):1253–1254.

Leroy, M., Winske, D., Goodrich, C., Wu, C. S., and Papadopoulos, K. (1982). The structure of perpendicular bow shocks. *Journal of Geophysical Research: Space Physics*, 87(A7):5081–5094.

Lovell, E. A., Goldstein, J., Valek, P. W., Spence, H. E., and Reeves, G. D. (2020). Evolution of the ring current during geomagnetic storms based on van allen probes observations. *Journal of Geophysical Research: Space Physics*, 125(2):e2019JA027403.

Martiningrum, D. R., Yamamoto, M., and Pradipta, R. (2022). Day-to-day variability of field-aligned irregularities occurrence in nighttime f-region ionosphere over the equatorial atmosphere radar: A combinatorics analysis. *Authorea Preprints*.

Maruyama, N., Richmond, A., Fuller-Rowell, T., Codrescu, M., Sazykin, S., Toffoletto, F., Spiro, R., and Millward, G. (2005). Interaction between direct penetration and disturbance dynamo electric fields in the storm-time equatorial ionosphere. *Geophysical Research Letters*, 32(17).

Matamba, T. M. and Habarulema, J. B. (2018). Ionospheric responses to cme-and cir-driven geomagnetic storms along 30 e–40 e over the african sector from 2001 to 2015. *Space weather*, 16(5):538–556.

Memarzadeh, Y. (2009). *Ionospheric modeling for precise GNSS applications*. Citeseer.

Menvielle, M. and Berthelier, A. (1991). The kp index: A comprehensive review. *Annales Geophysicae*, 9(6):431–441.

Misra, P. and Enge, P. (2006). *Global Positioning System: Signals, Measurements, and Performance*. Ganga-Jamuna Press, 2nd edition.

Olson, P. and Christensen, U. R. (2006). Dipole moment scaling for convection-driven planetary dynamos. *Earth and Planetary Science Letters*, 250(3-4):561–571.

Owens, M. J. and Forsyth, R. J. (2013). The heliospheric magnetic field. *Living Reviews in Solar Physics*, 10(1):5.

Parker, E. (1965). Dynamical theory of the solar wind. *Space Science Reviews*, 4(5):666–708.

Parker, E. N. (1958). Dynamics of the interplanetary gas and magnetic fields. *Astrophysical Journal*, 128:664–676.

Perkins, F. (1975). Ion-streaming instabilities: Electromagnetic and electrostatic. Technical report, Princeton Plasma Physics Lab.(PPPL), Princeton, NJ (United States).

Pi, X., Mendillo, M., Hughes, W. J., Buonsanto, M. J., Sipler, D. P., Kelly, J., Zhou, Q., Lu, G., and Hughes, T. J. (2000). Dynamical effects of geomagnetic storms and substorms in the middle-latitude ionosphere: An observational campaign. *Journal of Geophysical Research: Space Physics*, 105(A4):7403–7417.

Piddington, J. (1964). Geomagnetic storms, auroras and associated effects. *Space Science Reviews*, 3:724–780.

Praveena, K., Kumar, P. N., Reddy, D. K., and Santhosh, N. (2020). Analysis of ionospheric scintillations of navic l5 and s-band signals over low latitude indian region. *Procedia Computer Science*, 171:989–998.

Prölss, G. W. and Prölss, G. W. (2004). Interplanetary medium. *Physics of the Earth's Space Environment: An Introduction*, pages 277–347.

Pudovkin, M. and Semenov, V. (1985). Magnetic field reconnection theory and the solar wind—magnetosphere interaction: A review. *Space Science Reviews*, 41(1):1–89.

Pulkkinen, A., Rastätter, L., Kuznetsova, M., Hesse, M., Ridley, A., Raeder, J., Singer, H., and Chulaki, A. (2010). Systematic evaluation of ground and geostationary magnetic field predictions generated by global magnetohydrodynamic models. *Journal of Geophysical Research: Space Physics*, 115(A3).

Ratcliffe, J. (1972). An introduction to the ionosphere and magnetosphere. *Cambridge University Press*.

Rishbeth, H. (1971). Polarization fields produced by winds in the equatorial f-region. *Planetary and Space Science*, 19(3):357–369.

Russell, C. (2000). The solar wind interaction with the earth's magnetosphere: A tutorial. *IEEE transactions on plasma science*, 28(6):1818–1830.

Salles, L. A., Vani, B. C., Moraes, A., Costa, E., and de Paula, E. R. (2021). Investigating ionospheric scintillation effects on multifrequency gps signals. *Surveys in Geophysics*, 42(4):999–1025.

Schunk, R. W. and Nagy, A. F. (2009). *Ionospheres: Physics, Plasma Physics, and Chemistry*. Cambridge University Press, 2nd edition.

Singh, R. (2019). Coupling of the solar driven prolonged and transient processes to the equitorial and low latitude ionosphere. *Indian Institute of Geomagnetism*.

Spogli, L., Alfonsi, L., De Franceschi, G., Romano, V., Aquino, M., and Dodson, A. (2009). Climatology of gps ionospheric scintillations over high and mid-latitude european regions. In *Annales Geophysicae*, volume 27, pages 3429–3437. Copernicus Publications Göttingen, Germany.

Sugiura, M. and Iyemori, T. (2014). The dst index 1957–2009: Its derivation and scientific applications. *Annales Geophysicae*, 32(3):383–398.

Tandberg-Hanssen, E. (1995). Solar prominences. *Space Science Reviews*, 71(1-4):69–98.

Tandra, R. and Sahai, A. (2008). Noise calibration, delay coherence and snr walls for signal detection. In *2008 3rd IEEE Symposium on New Frontiers in Dynamic Spectrum Access Networks*, pages 1–11. IEEE.

Thomas, R. J. and Teske, R. G. (1971). Solar soft x-rays and solar activity: Ii. soft x-ray emission during solar flares. *Solar Physics*, 16:431–453.

Thomson, N. R. and Clilverd, M. A. (2005). Solar flare-induced ionospheric d-region enhancements from vlf phase and amplitude observations. *Journal of Atmospheric and Solar-Terrestrial Physics*, 67(10):877–886.

Treumann, R. A. and Baumjohann, W. (1997). *Advanced space plasma physics*, volume 30. Imperial College Press London.

Tsurutani, B., Mannucci, A., Iijima, B., Abdu, M. A., Sobral, J. H. A., Gonzalez, W., Guarnieri, F., Tsuda, T., Saito, A., Yumoto, K., et al. (2004). Global dayside ionospheric uplift and enhancement associated with interplanetary electric fields. *Journal of Geophysical Research: Space Physics*, 109(A8).

Tsurutani, B., Wu, S., Zhang, T., and Dryer, M. (2003). Coronal mass ejection (cme)-induced shock formation, propagation and some temporally and spatially developing shock parameters relevant to particle energization. *Astronomy & Astrophysics*, 412(1):293–304.

Tsurutani, B. T., Gonzalez, W. D., Tang, F., and Lee, Y. T. (1992). Great magnetic storms. *Geophysical Research Letters*, 19(1):73–76.

Tsurutani, B. T., Verkhoglyadova, O., Mannucci, A., Saito, A., Araki, T., Yumoto, K., Tsuda, T., Abdu, M. A., Sobral, J. H. A., Gonzalez, W. D., et al. (2008). Prompt penetration electric fields (ppefs) and their ionospheric effects during the great magnetic storm of 30–31 october 2003. *Journal of Geophysical Research: Space Physics*, 113(A5).

Van Dierendonck, A., Klobuchar, J., and Hua, Q. (1993). Ionospheric scintillation monitoring using commercial single frequency c/a code receivers. *Proceedings of ION GPS*, 93:1333–1342.

Wang, C.-P., Lyons, L. R., Nagai, T., Weygand, J. M., and McEntire, R. W. (2007). Sources, transport, and distributions of plasma sheet ions and electrons and dependences on interplanetary parameters under northward interplanetary magnetic field. *Journal of Geophysical Research: Space Physics*, 112(A10).

Waters, C. and Cox, S. (2009). Ulf wave effects on high frequency signal propagation through the ionosphere. In *Annales Geophysicae*, volume 27, pages 2779–2788. Copernicus Publications Göttingen, Germany.

Williams, D. J. (1985). Dynamics of the earth's ring current: Theory and observation. *Space Science Reviews*, 42(3-4):375–386.

Wu, J., Yang, G., Zhang, Y., Zhou, C., and Zhao, Z. (2019). Detection of daytime ionospheric irregularities at low latitudes with a multistatic hf radar. *IEEE Geoscience and Remote Sensing Letters*, 16(6):839–843.

Yamada, M., Kulsrud, R., and Ji, H. (2010). Magnetic reconnection. *Reviews of modern physics*, 82(1):603–664.

Yeh, K. C. and Liu, C.-H. (1982). Radio wave scintillations in the ionosphere. *Proceedings of the IEEE*, 70(4):324–360.

Yizengaw, E., Doherty, P., Zesta, E., Carter, B. A., Lawal, O., and Baki, P. Response of the equatorial ionophere to the geomagnetic storm of 22 june 2015 in the african sector. *Geophysical Research Letters*, 43(11):5193–5200.

Yokoyama, N. and Kamide, Y. (1997). Statistical nature of geomagnetic storms. *Journal of Geophysical Research: Space Physics*, 102(A7):14215–14222.